

Accepted Manuscript

On the simulation of wave propagation with a higher-order finite volume scheme based on Reproducing Kernel Methods

X. Nogueira, I. Colominas, L. Cueto-Felgueroso, S. Khelladi

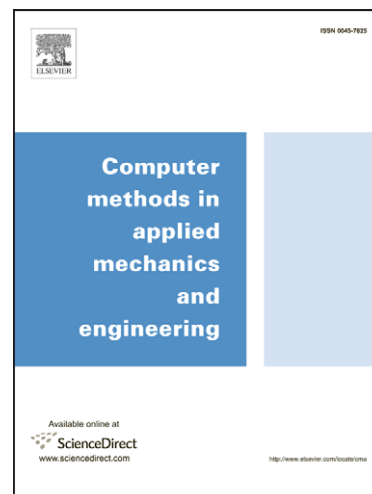
PII: S0045-7825(09)00421-6
DOI: [10.1016/j.cma.2009.12.015](https://doi.org/10.1016/j.cma.2009.12.015)
Reference: CMA 9124

To appear in: *Comput. Methods Appl. Mech. Engrg.*

Received Date: 18 May 2009
Revised Date: 18 December 2009
Accepted Date: 22 December 2009

Please cite this article as: X. Nogueira, I. Colominas, L. Cueto-Felgueroso, S. Khelladi, On the simulation of wave propagation with a higher-order finite volume scheme based on Reproducing Kernel Methods, *Comput. Methods Appl. Mech. Engrg.* (2009), doi: [10.1016/j.cma.2009.12.015](https://doi.org/10.1016/j.cma.2009.12.015)

This is a PDF file of an unedited manuscript that has been accepted for publication. As a service to our customers we are providing this early version of the manuscript. The manuscript will undergo copyediting, typesetting, and review of the resulting proof before it is published in its final form. Please note that during the production process errors may be discovered which could affect the content, and all legal disclaimers that apply to the journal pertain.



1
2
3
4
5
6
7
8
9
10
11
12
13
14
15
16
17
18
19
20
21
22
23
24
25
26

On the simulation of wave propagation with a higher-order finite volume scheme based on Reproducing Kernel Methods

X. Nogueira^a, I. Colominas^{*,a}, L. Cueto-Felgueroso^b, S. Khelladi^c

^a*Group of Numerical Methods in Engineering, Dept. of Applied Mathematics,
Universidade da Coruña. Campus de Elviña, 15071, A Coruña, Spain*

^b*Dept. of Civil and Environmental Engineering, Massachusetts Institute of Technology,
77 Massachusetts Ave, Cambridge, MA 02139, USA*

^c*Arts et Métiers ParisTech, 151 boulevard de l'Hôpital, 75013 Paris, France*

Abstract

27
28
29
30
31
32
33
34
35
36
37
38
39
40
41
42
43
44
45
46
47

In this work we study the dispersion and dissipation characteristics of a higher-order Finite Volume Method based on Moving Least Squares approximations (FV-MLS), and we analyze the influence of the kernel parameters on the properties of the scheme. Several numerical examples are included. The results clearly show a significant improvement of dispersion and dissipation properties of the numerical method if the third-order FV-MLS scheme is used compared with the second-order one. Moreover, with the explicit fourth-order Runge-Kutta scheme the dispersion error is lower than with the third-order Runge-Kutta scheme, whereas the dissipation error is similar for both time-integration schemes. It is also shown that a CFL number lower than 0.8 is required to avoid an unacceptable dispersion error.

Key words: High-order methods, Moving Least Squares, Dispersion and dissipation characteristics

1. Introduction

48
49
50
51
52
53
54
55

The resolution of wave propagation problems is a challenging work for numerical methods. The solution we want to approximate usually presents a wide spectrum of frequencies, and the numerical scheme has to be accurate

^{*}Corresponding author, e-mail: icolominas@udc.es

1
2
3
4
5
6
7
8
9
10
11
12
13
14
15
16
17
18
19
20
21
22
23
24
25
26
27
28
29
30
31
32
33
34
35
36
37
38
39
40
41
42
43
44
45
46
47
48
49
50
51
52
53
54
55
56
57
58
59
60
61
62
63
64
65

enough to preserve the shape and frequency of propagating waves. It is also usual to face with nonlinear interactions and complex geometries. In order to accurately solve this kind of problems, the numerical scheme should introduce the minimal dispersion and dissipation errors.

Computation of derivatives is a crucial point to assess the quality of a numerical scheme. Although a higher-order discretization usually means greater accuracy, it is not always true, specially for shorter waves relative to grid size [1]. Thus, it is possible to develop numerical schemes optimized to solve a wider range of the spectrum of frequencies [2, 3, 4, 5, 6]. In these methods, the number of available coefficients to perform the optimization process is increased by decreasing the order of the approximation. Thus, it is possible to develop numerical methods with higher spectral resolution than other higher-order discretizations.

However, the use of structured grids on complex geometries may lead to distort elements that affect greatly to the accuracy of the numerical method. For these geometries, it could be interesting the use of unstructured grids. However, most of the high-accurate methods developed for structured grids do not work on unstructured or distorted grids.

On this kind of grids it is difficult to increase the spectral resolution of a given numerical scheme by using methodologies different than raising the order of the numerical scheme, due to the difficulty in generalizing the methods developed for structured meshes. Some approaches have been developed for the construction of accurate methods to solve wave propagation on unstructured grids [7, 8, 9, 10, 11, 12, 13, 14, 15, 16, 17, 18]. The finite volume method is well suited for the computation of wave transport problems, particularly for the non-linear case, where finite difference approaches may fail [19]. Moreover, this method can be applied on unstructured grids, but the way for increasing the order of the scheme on these grids is not obvious. The main problem is the evaluation of high-order derivatives.

The FV-MLS method [20, 21, 22, 23, 24] overcomes the difficulty in the computation of high-order derivatives by using the Moving Least Squares (MLS) technique [25]. This scheme builds higher-order schemes in a finite volume framework without the introduction of new degrees of freedom. One of the advantages of this numerical method is its good performance on unstructured grids, due to the accurate and multidimensional nature of MLS reconstructions. Thus, the FV-MLS method has successfully been applied to Euler (and Linearized Euler) and Navier-Stokes equations, shallow water equations and also to Cahn-Hilliard and Kuramoto-Sivashinsky type of

equations.

One of the key points in the development of the FV-MLS method is the kernel function. In this work we present the first analysis of the influence of the kernel parameters on the dispersion and dissipation characteristics of the FV-MLS method. In particular, we analyze the behavior of the FV-MLS method with two kinds of kernels: the cubic spline kernel and the exponential kernel.

Section 2 is devoted to present the fundamentals of the Finite volume method based on Moving Least Squares approximations. Section 3 analyzes the influence of the kernel parameters on the MLS-shape functions and its derivatives. In section 4 we study the influence of kernel parameters in the computation of discrete differential operators by using MLS, and then, in section 5, we analyze the discretization of the one-dimensional linear equation with the third-order FV-MLS method. In section 6 we study the influence of kernel parameters on the discretization of elliptic and hyperbolic terms. In section 7 we present two 1D numerical examples for the linear and the non-linear case, with the purpose of showing the performance of the proposed methodology. Moreover, a 2D case computed using an unstructured grid is presented, to check the validity of the 1D analysis to more general problems. Finally, conclusions are drawn on section 8.

2. Numerical method: A MLS-based Finite Volume scheme

A method based on the application of Moving Least Squares [25] to compute the derivatives in a finite volume framework (FV-MLS) has been developed in [20, 21, 22]. In order to increase the order achieved by the finite volume method, a Taylor expansion of the variable is performed at the interior of each cell. The approximation of the higher order derivatives needed to compute the Taylor reconstruction is obtained by a Moving Least Squares approach.

Thus, if we consider a function $\Phi(\mathbf{x})$ defined in a domain Ω , the basic idea of the MLS approach is to approximate $\Phi(\mathbf{x})$, at a given point \mathbf{x} , through a weighted least-squares fitting of $\Phi(\mathbf{x})$ in a neighborhood of \mathbf{x} as

$$\Phi(\mathbf{x}) \approx \widehat{\Phi}(\mathbf{x}) = \sum_{i=1}^m p_i(\mathbf{x}) \alpha_i(\mathbf{z}) \Big|_{\mathbf{z}=\mathbf{x}} = \mathbf{p}^T(\mathbf{x}) \boldsymbol{\alpha}(\mathbf{z}) \Big|_{\mathbf{z}=\mathbf{x}} \quad (1)$$

$\mathbf{p}^T(\mathbf{x})$ is an m -dimensional (usually polynomial) basis and $\boldsymbol{\alpha}(\mathbf{z}) \Big|_{\mathbf{z}=\mathbf{x}}$ is a set

of parameters to be determined, such that they minimize the following error functional:

$$J\left(\boldsymbol{\alpha}(\mathbf{z})\Big|_{\mathbf{z}=\mathbf{x}}\right) = \int_{\mathbf{y} \in \Omega_{\mathbf{x}}} W(\mathbf{z} - \mathbf{y}, h)\Big|_{\mathbf{z}=\mathbf{x}} \left[\Phi(\mathbf{y}) - \mathbf{p}^T(\mathbf{y})\boldsymbol{\alpha}(\mathbf{z})\Big|_{\mathbf{z}=\mathbf{x}} \right]^2 d\Omega_{\mathbf{x}} \quad (2)$$

being $W(\mathbf{z} - \mathbf{y}, h)\Big|_{\mathbf{z}=\mathbf{x}}$ a *kernel* with compact support (denoted by $\Omega_{\mathbf{x}}$) centered at $\mathbf{z} = \mathbf{x}$. The parameter h is the smoothing length, which is a measure of the size of the support $\Omega_{\mathbf{x}}$ [20].

In this work the following polynomial cubic basis is used:

$$\mathbf{p}(\mathbf{x}) = (1 \quad x \quad y \quad xy \quad x^2 \quad y^2 \quad x^2y \quad xy^2 \quad x^3 \quad y^3)^T \quad (3)$$

which provides cubic completeness. In the above expression, (x, y) denotes the Cartesian coordinates of \mathbf{x} . From a practical point of view, for each point I we need to define a set of neighbors inside the compact support $\Omega_{\mathbf{x}}$. Following [20], the interpolation structure can be identified as

$$\widehat{\Phi}_I(\mathbf{x}) = \mathbf{p}^T(\mathbf{x})\boldsymbol{\alpha}(\mathbf{z})\Big|_{\mathbf{z}=\mathbf{x}} = \mathbf{p}^T(\mathbf{x})\mathbf{M}^{-1}(\mathbf{x})\mathbf{P}_{\Omega_{\mathbf{x}}}\mathbf{W}(\mathbf{x})\boldsymbol{\Phi}_{\Omega_{\mathbf{x}}} = \mathbf{N}^T(\mathbf{x})\boldsymbol{\Phi}_{\Omega_{\mathbf{x}}} \quad (4)$$

$$\widehat{\Phi}_I(\mathbf{x}) = \sum_{j=1}^{n_{\mathbf{x}_I}} N_j(\mathbf{x})\Phi_j \quad (5)$$

In the above, $n_{\mathbf{x}_I}$ is the number of neighbors of the cell I . Moreover, $\mathbf{M} = \mathbf{P}_{\Omega_{\mathbf{x}}}\mathbf{W}(\mathbf{x})\mathbf{P}_{\Omega_{\mathbf{x}}}^T$ is the moment matrix.

We also define the matrices (see [20]):

$$\mathbf{P}_{\Omega_{\mathbf{x}}} = \left(\mathbf{p}(x)_1 \cdots \mathbf{p}(x)_{n_{\mathbf{x}_I}} \right) \quad (6)$$

$$\boldsymbol{\Phi}_{\Omega_{\mathbf{x}}} = (\Phi(x_1) \cdots \Phi(x_{n_{\mathbf{x}_I}})) \quad (7)$$

and

$$\mathbf{W}(\mathbf{x}) = \text{diag}(W_i(\mathbf{x})) \quad i = 1, \dots, n_{\mathbf{x}_I}. \quad (8)$$

From equation (5), the approximation is written in terms of the MLS “shape functions” $\mathbf{N}^T(\mathbf{x})$.

$$\mathbf{N}^T(\mathbf{x}) = \mathbf{p}^T(\mathbf{x})\mathbf{M}^{-1}(\mathbf{x})\mathbf{P}_{\Omega_{\mathbf{x}}}\mathbf{W}(\mathbf{x}) \quad (9)$$

In order to improve the conditioning, the polynomial basis (3) is locally defined and scaled: if the shape functions are evaluated at \mathbf{x}_I , the polynomial basis is evaluated at $(\mathbf{x} - \mathbf{x}_I)/h$. Thus, shape functions evaluated at \mathbf{x}_I read:

$$\mathbf{N}^T(\mathbf{x}_I) = \mathbf{p}^T(\mathbf{0})\mathbf{M}^{-1}(\mathbf{x}_I)\mathbf{P}_{\Omega_{\mathbf{x}_I}}\mathbf{W}(\mathbf{x}_I) = \mathbf{p}^T(\mathbf{0})\mathbf{C}(\mathbf{x}_I) \quad (10)$$

we define the matrix $\mathbf{C}(\mathbf{x})$ as:

$$\mathbf{C}(\mathbf{x}) = \mathbf{M}^{-1}(\mathbf{x})\mathbf{P}_{\Omega_{\mathbf{x}}}\mathbf{W}(\mathbf{x}) \quad (11)$$

The derivatives of $\mathbf{N}^T(\mathbf{x})$ can be used to compute an approximation to the derivatives of the function. So, the gradient of $\widehat{\Phi}(\mathbf{x})$ is evaluated as

$$\nabla\widehat{\Phi}(\mathbf{x}) = \sum_{j=1}^{n_{\mathbf{x}_I}} \Phi_j \nabla N_j(\mathbf{x}) \quad (12)$$

In a context of generalized Godunov's methods we use equation (12) to compute the first and second derivatives required for the Taylor reconstruction of the variables at quadrature points at the edges. Elliptic terms, like viscous terms in the Navier-Stokes equations, are computed directly using MLS approximations. In case of unsteady problems, this reconstruction needs to use correction terms in order to ensure that the average value of the reconstructed variables over a cell I is the centroid value \mathbf{U}_I [8, 20, 21, 22]. The resulting scheme is a third-order method.

The neighbors of each cell centroid I of the grid are the centroids of the neighboring cells. For boundary cells, we add nodes (ghost nodes) placed in the middle of the edge defining the boundary. The definition of the stencil for each cell is done at the beginning of the calculations. It is possible to use different kernels for the definition of shape functions. We have considered two of them: the cubic spline kernel and the exponential kernel. The 1D cubic kernel is given by:

$$W(d) = \begin{cases} 1 - \frac{3}{2}d^2 + \frac{3}{4}d^3 & d \leq 1 \\ \frac{1}{4}(2-d)^3 & 1 < d \leq 2 \\ 0 & d > 2 \end{cases} \quad (13)$$

In equation (13) $d = \frac{|x_j - x^*|}{h}$, and $h = k \max(|x_j - x^*|)$ with $j = 1, \dots, n_{x^*}$. We call x^* to the reference point (the point where the MLS-shape functions

are evaluated), and n_{x^*} is the number of neighbors of the reference point. The exponential kernel may be defined in 1D as:

$$W(x, x^*, s_x) = \frac{e^{-\left(\frac{d}{c}\right)^2} - e^{-\left(\frac{d_m}{c}\right)^2}}{1 - e^{-\left(\frac{d_m}{c}\right)^2}} \quad (14)$$

with $d = |x_j - x^*|$, $d_m = 2 \max(|x_j - x^*|)$, with $j = 1, \dots, n_{x^*}$, $c = \frac{d_m}{s_x}$, x is the position of every cell centroid of the stencil and s_x is a shape parameter. A 2D kernel is obtained by multiplying two 1D kernels. Thus, the 2D exponential kernel is the following:

$$W_j(\mathbf{x}, \mathbf{x}^*, s_x, s_y) = W_j(x, x^*, s_x)W_j(y, y^*, s_y) \quad (15)$$

More details about the FV-MLS method can be found in [20, 21, 22].

3. Influence of kernel parameters on the MLS-shape functions and its derivatives

In section 2, we have exposed that the derivatives needed in the reconstruction step of the finite volume method are computed by using MLS shape functions. Thus, MLS shape functions are going to play a crucial role in the accuracy of this method. In this section we perform a 1D study of the influence of the choice of the different parameters defining the kernel function. It is possible to find a great amount of kernel functions [26], but here we only focus on the kernels defined by (13) and (15).

We consider a 5-point stencil, namely $-2, -1, 0, +1, +2$, where 0 is the point where we compute the derivative (figure 1). We also consider equally-spaced points. The number of points of the stencil also has an influence on the behavior of the method, and also the basis $\mathbf{p}(\mathbf{x})$. However, in this work we focus on the 5-point stencil and the cubic polynomial basis. The reason is that the polynomial cubic basis is the usual choice in the implementation of the third-order FV-MLS method, and five is the maximum number of elements in one direction when multidimensional stencils are used with the third-order FV-MLS method [20, 21, 22]. Clearly, the results of the present study no longer holds for the case of arbitrary distributions of points, but we will be able to get a flavor of the behavior of the scheme in this cases, as it will be shown in the numerical examples.

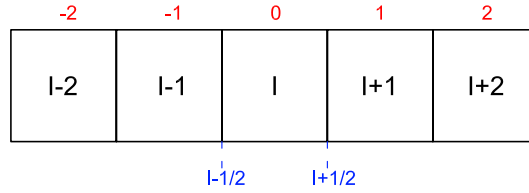


Figure 1: Spatial discretization scheme.

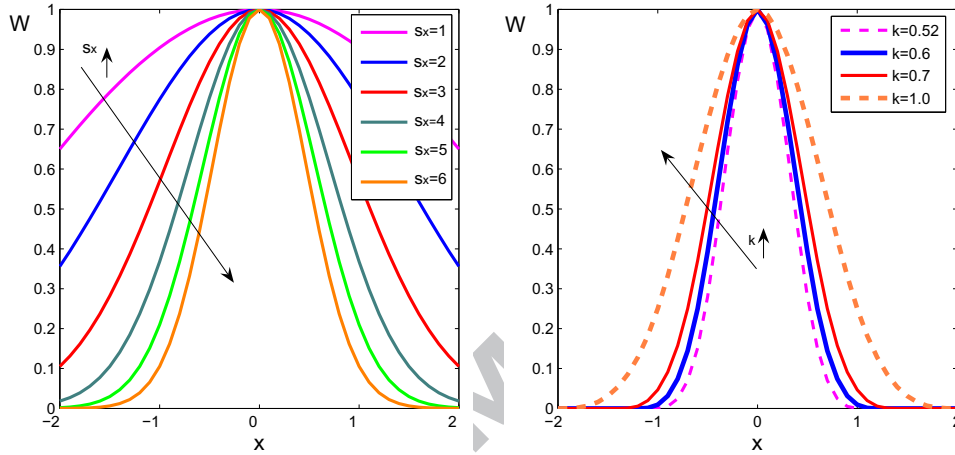


Figure 2: Shape of the kernel function for different choices of the defining parameters. On the left, we show the results for the exponential kernel(15) when the parameter s_x is modified. On the right we plot the results for the cubic spline (13) when we vary the k parameter defining the smoothing length h .

As parameters for modifying the kernels, we have chosen k for the cubic spline (13) and s_x for the exponential kernel (15). A change of these parameters causes a modification in the shape of the kernels, as is plotted in figure 2. The shape variation as we change the value of the parameter is bigger for the exponential kernel than for the cubic spline kernel. This feature of exponential kernel represents an advantage in terms of robustness for arbitrary meshes.

When we compute the derivatives with (12) we need to compute the derivative of the MLS shape functions. Thus, in figures 3, 4 and 5 we plot the value of $\frac{\partial N_j}{\partial x}$ in the points of the stencil ($j = -2, -1, 0, +1, +2$).

The values of the first derivative of the MLS shape functions computed with (13) do not depend on the value of the smoothing length (h). These values match with the coefficients of a fourth-order centered finite difference

discretization. The case of the exponential kernel is completely different. With this kernel the values obtained depend on the shape parameter s_x . We observe that for $s_x > 4$ these values tend to the values obtained with the cubic spline kernel. Moreover, for this value of s_x there is a change in the tendency of the evolution of the first derivative. The reason of this behavior relies on the fact that the derivative of (15) changes its tendency for a value of s_x next to four (figure 6).

From equation (10), the derivative of a MLS shape function can be written as:

$$\frac{\partial \mathbf{N}^T(\mathbf{x})}{\partial x} = \frac{\partial \mathbf{p}^T(\mathbf{0})}{\partial x} \mathbf{C}(\mathbf{x}) + \mathbf{p}^T(\mathbf{0}) \frac{\partial \mathbf{C}(\mathbf{x})}{\partial x} \quad (16)$$

where the derivative of \mathbf{C} is:

$$\frac{\partial \mathbf{C}(x)}{\partial x} = \mathbf{C}(x) \mathbf{W}^{-1} \frac{\partial \mathbf{W}(x)}{\partial x} (\mathbf{I} - \mathbf{P}_{\Omega x} \mathbf{C}(x)) \quad (17)$$

Equations (16) and (17) show the influence of the derivative of the kernel on the MLS-shape function. In figure 6 we plot the evolution of the kernel derivative when we modify the kernel parameters. We observe that for nodes 1, 2, -2, -1 the tendency of the evolution changes when the value of s_x is between 3 and 4.

In figure 4 we plot the variation of the second derivative of the MLS shape functions. In this case, the influence of the parameters is bigger than for the first derivative for both the exponential kernel and the cubic spline kernel. Third derivative of the MLS shape functions is independent of the kernel parameters (see figure 5).

4. Influence of kernel parameters on the discrete differential operators

In this section we analyze the dispersion and dissipation properties of the discrete differential operators obtained with MLS approximations.

Let us consider a periodic function $u(x)$ in a domain $[0, L]$. Then, $u(x)$ is decomposed in a discrete Fourier series as follows:

$$u(x) = \sum_{q=-\frac{M}{2}}^{\frac{M}{2}-1} f_q e^{i\kappa_q x} \quad (18)$$

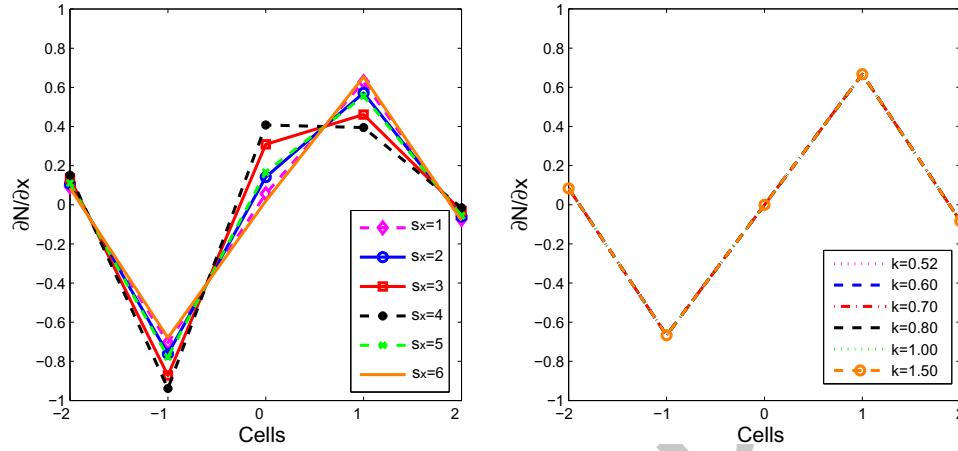


Figure 3: Variation of the values of the first derivative of the MLS shape function N with the parameters of the kernel function. On the left we plot the results for the exponential kernel (15), when we vary s_x . On the right, we show the results for the cubic kernel (13), when we vary the parameter k .

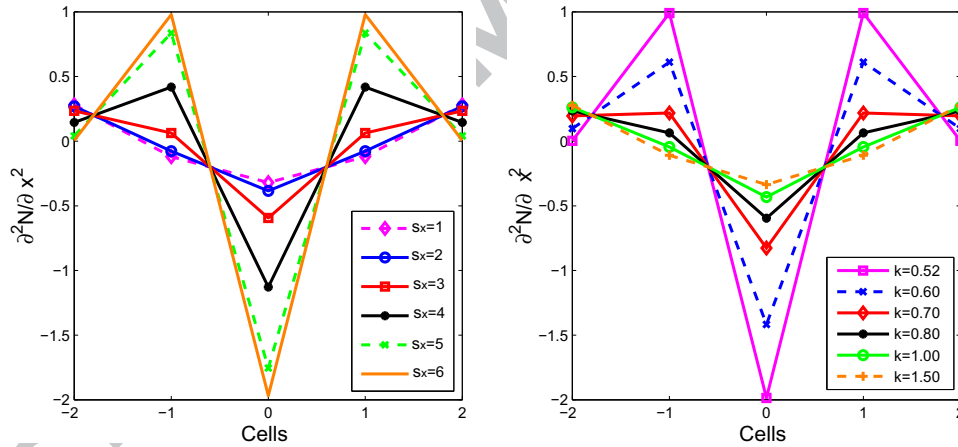


Figure 4: Variation of the values of the second derivative of the MLS shape function N with the parameters of the kernel function. On the left we plot the results for the exponential kernel (15), when we vary s_x . On the right, we show the results for the cubic kernel (13), when we vary the parameter k .

where $\kappa_q = \frac{2\pi q}{\Delta x M}$ is the *wavenumber*, $\Delta x = \frac{L}{M}$, $i = \sqrt{-1}$ and f_q are the

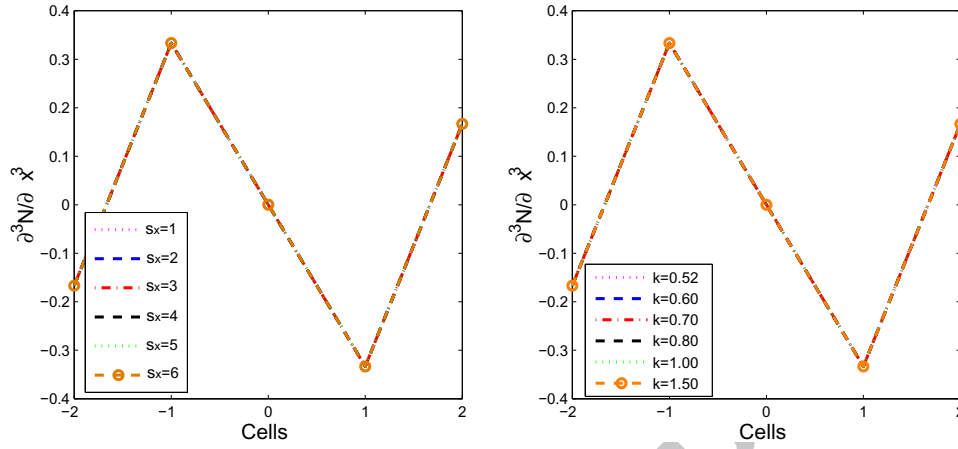


Figure 5: Variation of the values of the third derivative of the MLS shape function N with the parameters of the kernel function. On the left we plot the results for the exponential kernel (15), when we vary s_x . On the right, we show the results for the cubic kernel (13), when we vary the parameter k .

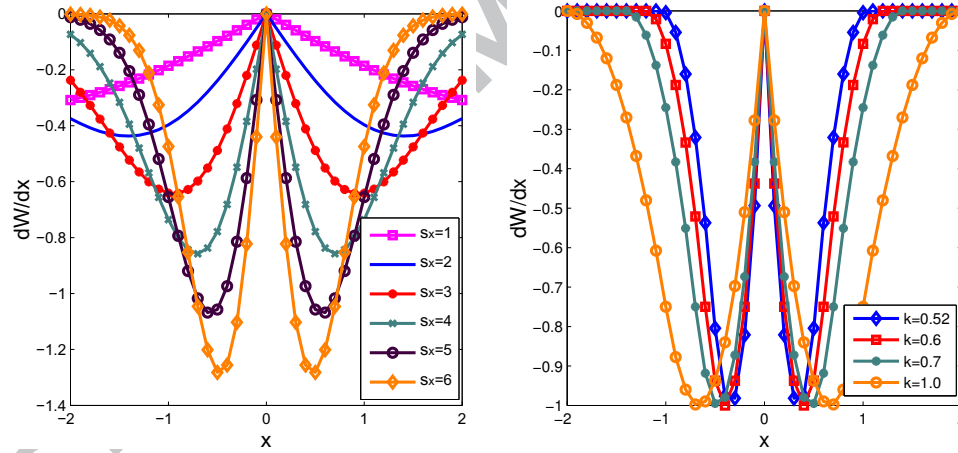


Figure 6: Variation of the values of the first derivative of the exponential kernel with s_x (left). On the right we plot the variation of the values of the first derivative of the cubic spline with k .

Fourier coefficients. If $u(x)$ is smooth enough, the exact derivative of (18) is

$$\frac{\partial u(x)}{\partial x} = \sum_{q=-\frac{M}{2}}^{\frac{M}{2}-1} f_q i \kappa_q e^{i \kappa_q x} \quad (19)$$

On the other hand, given a discrete set of points $x_j = j\Delta x$, $j = 1, 2, \dots, M$ we can write:

$$u(x_j) = \sum_{q=-\frac{M}{2}}^{\frac{M}{2}-1} f_q e^{i\kappa_q x_j} \quad (20)$$

For a MLS approximation of the derivative of $u(x_j)$, we write:

$$\begin{aligned} \left. \frac{\partial u}{\partial x} \right|_{x_j} &= \sum_{l=-P}^Q \frac{\partial N_{j+l}}{\partial x} u_{(x_j+l\Delta x)} = \\ &= \sum_{l=-P}^Q \frac{\partial N_{j+l}}{\partial x} \left[\sum_{q=-\frac{M}{2}}^{\frac{M}{2}-1} f_q e^{i\kappa_q (x_j+l\Delta x)} \right] = \\ &= \sum_{q=-\frac{M}{2}}^{\frac{M}{2}-1} f_q \left[\sum_{l=-P}^Q \frac{\partial N_{j+l}}{\partial x} e^{i\kappa_q (x_j+l\Delta x)} \right] = \\ &= \sum_{q=-\frac{M}{2}}^{\frac{M}{2}-1} f_q e^{i\kappa_q x_j} \left[\sum_{l=-P}^Q \frac{\partial N_{j+l}}{\partial x} e^{i\kappa_q (l\Delta x)} \right] = \sum_{q=-\frac{M}{2}}^{\frac{M}{2}-1} f_q i\kappa_q^* e^{i\kappa_q x_j} \quad (21) \end{aligned}$$

where P is the number of cells of the *stencil* on the left of cell 0 (figure 1) and Q is the number of cells on the right. Comparing with (19) the modified wave number (κ_q^*) of the numerical scheme is:

$$\kappa_q^* = (-i) \sum_{l=-P}^Q \frac{\partial N_{j+l}}{\partial x} e^{i\kappa_q (l\Delta x)} \quad (22)$$

The wavenumber is proportional to the frequency. Thus, the numerical scheme introduces a different error depending on the frequency of the wave. For certain frequencies the modified wavenumber coincide with the real wavenumber. These are the “resolved” frequencies for the numerical method. When the numerical wavenumber does not match with the real wavenumber *dispersion errors* appear. On the other hand, the amplitude error (*dissipation error*) is related to the imaginary part of the modified wavenumber of the numerical scheme [2]. It is convenient to introduce a scaled wavenumber $\kappa\Delta x$, on the domain $[0, \pi]$. In figure 7 we plot the real scaled wavenumber $\kappa\Delta x$

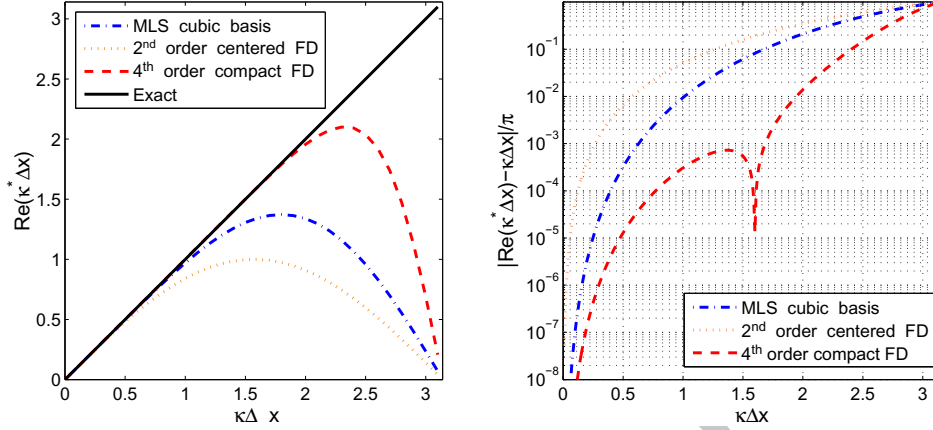


Figure 7: $\kappa^* \Delta x$ versus $\kappa \Delta x$ for different schemes. On the right we plot the magnitude of the dispersion error ($|Re(k^* \Delta x) - \kappa \Delta x|/\pi$).

versus the real part of the modified scaled wavenumber $\kappa^* \Delta x$ for three different numerical schemes: a second-order centered finite differences scheme, a fourth-order tridiagonal compact finite difference scheme (see [2]), and a MLS approximation with polynomial cubic basis. Figure 7 shows the spectral resolution of the represented numerical schemes. The curve of the modified wavenumber seems to be overlapped with the curve of real wavenumber in a range of frequencies. However this overlapping may be not perfect, but at this scale this is difficult (or impossible) to appreciate. But when the error is plotted in a logarithmic scale (as in the dispersion error curve) this appear as “dips”. The reason for this is that the numerical wavenumber is greater than the actual wavenumber through a portion of the wavenumber spectrum, and then it dips below. When the numerical wavenumber crosses through the actual wavenumber, they are equal and the error is zero, causing the “dip” in figure 7 (right).

We remark that the variation of the parameters of the kernel function (k, s_x) does not influence the dispersion properties of the MLS approximation (for the stencil plotted in figure 1). Moreover, the dispersion curve matches with the dispersion curve of a fourth-order centered finite differences (non-compact). On the other hand, the imaginary part of the modified wavenumber (22) of the MLS approximation with the cubic spline kernel (13) is null. However, when we use the exponential kernel the imaginary part is not null. As the imaginary part is related to the dissipation error, we con-

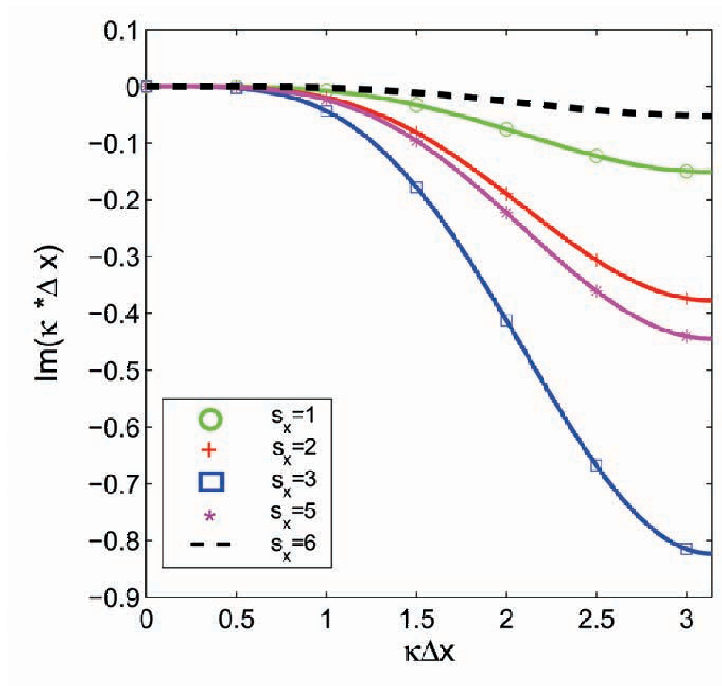


Figure 8: Imaginary part of the modified wavenumber of the MLS approximations with the exponential kernel for different values of s_x . A zero value indicates that there is no introduction of dissipation.

clude that the use of the exponential kernel introduces more dissipation than the cubic kernel.

We note that for the computations of figures 7 and 8 we have considered the 5-points centered stencil plotted in figure 1, so then $P = Q = 2$.

The previous analysis of the discrete MLS operator indicates the behavior of the MLS approximation to the computation of elliptic terms (viscous terms) in the Navier-Stokes equations when computed with MLS shape functions (see [20]).

5. 1D linear advection equation analysis

Now, we examine the behavior of the FV-MLS method [20, 21, 22] in the computation of hyperbolic terms. We study the resolution of the 1D linear advection equation:

$$\frac{\partial u}{\partial t} + a \frac{\partial u}{\partial x} = 0 \quad (23)$$

on the domain $0 \leq x \leq 2\pi$, with an harmonic wave as initial condition:

$$u(x, 0) = g(0)e^{ikx} \quad (24)$$

and that also verifies that $u(0) = u(2\pi)$. In equation (23), u is a scalar quantity propagating with phase velocity a . In order to make the exposition easier to follow, we consider only $a > 0$. However, the conclusions will be valid for any value of a .

With this initial setup, the solution of the problem is written as:

$$u(x, t) = g(t)e^{ikx} \quad (25)$$

Thus, introducing (25) in (23):

$$\frac{dg}{dt}e^{ikx} + ia\kappa g e^{ikx} = 0 \quad (26)$$

that is,

$$\frac{dg}{dt} = -ia\kappa g \quad (27)$$

and consequently $g(t)$ is

$$g(t) = g(0)e^{-ia\kappa t} \quad (28)$$

where $g(0)$ is the initial value of $g(t)$. Thus, we have:

$$u(x, t) = g(0)e^{i(\kappa x - a\kappa t)} \quad (29)$$

On the other hand, an arbitrary initial wave can be obtained by the addition of initial conditions of the form (24):

$$u(x, 0) = \sum_{q=1}^F g_q(0)e^{i\kappa_q x} \quad (30)$$

where F is the number of Fourier modes.

Due to the linearity of equation (23), the solution can be obtained by the addition of solutions of the form (29). Thus, for F modes we obtain:

$$u(x, t) = \sum_{q=1}^F g_q(0)e^{i\kappa_q(x-at)} \quad (31)$$

1
2
3
4
5
6
7
8
9
10
11
12
13
14
15
16
17
18
19
20
21
22
23
24
25
26
27
28
29
30
31
32
33
34
35
36
37
38
39
40
41
42
43
44
45
46
47
48
49
50
51
52
53
54
55
56
57
58
59
60
61
62
63
64
65

A real wavenumber κ is related to a real frequency $\omega = a\kappa$, such as the equation (31) is a solution of (23). The relationship between frequency and wavenumber is called *dispersion relation*. For equation (23) this relationship is linear, that is a characteristic feature of wave propagation in non-dispersive media. Thus, the phase velocity is the same for all the wavenumbers.

The discretization of equation (23) usually introduces a dispersion error. This means that in the numerical solution of (23), waves with different wavenumber propagate with different velocities. Moreover, if the modified wavenumber is complex, dissipation errors will appear.

In the following, we expose the analysis of the discretization of the equation (23) with the third-order FV-MLS method. This analysis will allow us to evaluate the behavior of the FV-MLS method in the approximation of convective terms of a transport equation. We start with the analysis of the spatial discretization only, without taking into account the effects of time integration. The analysis of the complete discretization will be exposed in the section 6.2.1.

As the solution is linear, we perform the analysis for a single Fourier mode (equation (30)), so the subindex q is omitted.

Different from a finite difference discretization, where we use point values of the variable, a finite volume scheme refers to the mean value of the variables inside a control volume I .

$$\tilde{u}_I = \frac{1}{\Delta x} \int_{x_L}^{x_R} u \, dx \quad (32)$$

where x_R and x_L are the values of the x -coordinate of the cell I interfaces $I + \frac{1}{2}$ and $I - \frac{1}{2}$, as is plotted in figure 1. Introducing (25) in (30), and by integration, we obtain:

$$\tilde{u}_I = \frac{g(t)}{i\kappa\Delta x} (e^{i\kappa(x_R)} - e^{i\kappa(x_L)}) \quad (33)$$

Then, writing (33) in terms of $g(0)$

$$\tilde{u}_I = \frac{g(0)}{i\kappa\Delta x} (e^{i\kappa(x_R-at)} - e^{i\kappa(x_L-at)}) \quad (34)$$

The FV-MLS method uses the integral form of equation (23):

$$\frac{\partial}{\partial t} \int_{x_L}^{x_R} u \, dx = - (f(x_R, t) - f(x_L, t)) \quad (35)$$

where $f(u) = au$ is the flux function.

Thus, by using the mean value definition (32) of $u(x)$, the spatial discretization of (35) reads as:

$$\frac{\partial \tilde{u}_I}{\partial t} = -\frac{a}{\Delta x} \left(u^*_{(I+\frac{1}{2})} - u^*_{(I-\frac{1}{2})} \right) \quad (36)$$

where u^* is the value of the variable reconstructed at the interfaces $(I+\frac{1}{2}, I-\frac{1}{2})$ (see figure 1). For the third order FV-MLS method we need a quadratic reconstruction of the variable at $I+\frac{1}{2}$:

$$u^*_{(I+\frac{1}{2})} = \tilde{u}_I + \frac{\partial \tilde{u}_I}{\partial x} \frac{\Delta x}{2} + \frac{1}{2} \frac{\partial^2 \tilde{u}_I}{\partial x^2} \left(\frac{\Delta x}{2} \right)^2 - TC_1^I + \vartheta (\Delta x^3) \quad (37)$$

TC_1^I is the correction term to guarantee the conservation of the mean [8, 20]:

$$TC_1^I = \frac{1}{2\Delta x} \frac{\partial^2 \tilde{u}_I}{\partial x^2} \int_I (x - x_I)^2 dx \quad (38)$$

Similarly, for $I-\frac{1}{2}$ we write:

$$u^*_{(I-\frac{1}{2})} = \tilde{u}_{(I-1)} + \frac{\partial \tilde{u}_{(I-1)}}{\partial x} \frac{\Delta x}{2} + \frac{1}{2} \frac{\partial^2 \tilde{u}_{(I-1)}}{\partial x^2} \left(\frac{\Delta x}{2} \right)^2 - TC_1^{(I-1)} + \vartheta (\Delta x^3) \quad (39)$$

with:

$$TC_1^{(I-1)} = \frac{1}{2\Delta x} \frac{\partial^2 \tilde{u}_{(I-1)}}{\partial x^2} \int_{(I-1)} (x - x_{(I-1)})^2 dx \quad (40)$$

Left hand side of (36) has the following exact value:

$$\frac{\partial \tilde{u}_I}{\partial t} = \frac{\partial g(t)}{\partial t} \frac{1}{\Delta x} \int_{x_L}^{x_R} e^{i\kappa x} dx = \frac{\partial g(t)}{\partial t} (e^{i\kappa x_R} - e^{i\kappa x_L}) \frac{1}{i\kappa \Delta x} \quad (41)$$

and, introducing (27) in (41) we can write:

$$\frac{\partial \tilde{u}_I}{\partial t} = \frac{-ag(t)}{\Delta x} (e^{i\kappa x_R} - e^{i\kappa x_L}) \quad (42)$$

The right hand side of (36) can be written as:

$$\begin{aligned}
\frac{a}{\Delta x} \left(u_{(I+\frac{1}{2})}^* - u_{(I-\frac{1}{2})}^* \right) &= \frac{a}{\Delta x} \left[\left(\tilde{u}_I + \frac{\partial \tilde{u}_I}{\partial x} \frac{\Delta x}{2} + \frac{1}{2} \frac{\partial^2 \tilde{u}_I}{\partial x^2} \left(\frac{\Delta x}{2} \right)^2 - TC_1^I \right) \right. \\
&- \left(\tilde{u}_{(I-1)} + \frac{\partial \tilde{u}_{(I-1)}}{\partial x} \frac{\Delta x}{2} + \frac{1}{2} \frac{\partial^2 \tilde{u}_{(I-1)}}{\partial x^2} \left(\frac{\Delta x}{2} \right)^2 - \right. \\
&\left. \left. - TC_1^{(I-1)} \right) + \vartheta (\Delta x^3) \right] \quad (43)
\end{aligned}$$

Next, we introduce the MLS approximation of derivatives,

$$\begin{aligned}
\frac{a}{\Delta x} \left(u_{(I+\frac{1}{2})}^* - u_{(I-\frac{1}{2})}^* \right) &= \frac{a}{\Delta x} \left[\tilde{u}_I - \tilde{u}_{(I-1)} + \right. \\
&+ \sum_{l=-P}^Q \frac{\partial N_{(I+l)}}{\partial x} \left(\tilde{u}_{(I+l\Delta x)} - \tilde{u}_{((I-1)+l\Delta x)} \right) \left(\frac{\Delta x}{2} \right) + \\
&+ \frac{1}{2} \sum_{l=-P}^Q \frac{\partial^2 N_{(I+l)}}{\partial x^2} \left[\tilde{u}_{(I+l\Delta x)} \left(\left(\frac{\Delta x}{2} \right)^2 - A \right) - \right. \\
&\left. \left. - \tilde{u}_{((I-1)+l\Delta x)} \left(\left(\frac{\Delta x}{2} \right)^2 - B \right) \right] + \vartheta (\Delta x^3) \right] \quad (44)
\end{aligned}$$

with

$$A = \frac{1}{\Delta x} \int_I (x - x_I)^2 dx, \quad B = \frac{1}{\Delta x} \int_{(I-1)} (x - x_{(I-1)})^2 dx \quad (45)$$

The equation (44) is obtained by assuming that all the control cells have the same length and a periodic domain. In that case, the set of MLS-shape functions is the same for every control volume, and $N_{I+l} = N_{(I-1)+l}$.

Introducing the equation (33) in (44), we write:

$$\begin{aligned}
\frac{-a}{\Delta x} \left(u_{(I+\frac{1}{2})}^* - u_{(I-\frac{1}{2})}^* \right) &= \frac{-ag(t)}{i\kappa\Delta x} \left(e^{i\kappa x_R} - e^{i\kappa x_L} \right) \left[1 - e^{-i\kappa\Delta x} + \right. \\
&+ \sum_{l=-P}^Q \frac{\partial N_{(I+l)}}{\partial x} \left(e^{i\kappa l\Delta x} - e^{i\kappa(l-1)\Delta x} \right) \left(\frac{\Delta x}{2} \right) + \\
&+ \frac{1}{2} \sum_{l=-P}^Q \frac{\partial^2 N_{(I+l)}}{\partial x^2} \left(\tilde{A} e^{i\kappa l\Delta x} - \tilde{B} e^{i\kappa(l-1)\Delta x} \right) + \\
&\left. + \vartheta (\Delta x^3) \right] \quad (46)
\end{aligned}$$

where \tilde{A} and \tilde{B} are:

$$\tilde{A} = \left(\frac{\Delta x}{2} \right)^2 - A \quad (47)$$

$$\tilde{B} = \left(\frac{\Delta x}{2} \right)^2 - B \quad (48)$$

Finally, we can write

$$\frac{-a}{\Delta x} \left(u_{(I+\frac{1}{2})}^* - u_{(I-\frac{1}{2})}^* \right) = \frac{-ag(t)}{i\kappa\Delta x} \left(e^{i\kappa x_R} - e^{i\kappa x_L} \right) Z_I \quad (49)$$

where we call Z_I to

$$\begin{aligned}
Z_I &= 1 - e^{-i\kappa\Delta x} + \\
&+ \sum_{l=-P}^Q \frac{\partial N_{(I+l)}}{\partial x} \left(e^{i\kappa l\Delta x} - e^{i\kappa(l-1)\Delta x} \right) \left(\frac{\Delta x}{2} \right) + \\
&+ \frac{1}{2} \sum_{l=-P}^Q \frac{\partial^2 N_{(I+l)}}{\partial x^2} \left(\tilde{A} e^{i\kappa l\Delta x} - \tilde{B} e^{i\kappa(l-1)\Delta x} \right) + \vartheta (\Delta x^3)
\end{aligned} \quad (50)$$

We note that we have obtained the equations (42) and (49) from the left hand side and the right hand side of the equation (36). Thus, the wavenumber is:

$$\kappa = \frac{Z_I}{i} \quad (51)$$

Now, we define Z^* as the approximation (50) of Z_I including quadratic terms. Thus, the modified wavenumber can be written as:

$$\kappa^* = \frac{Z^*}{i} \quad (52)$$

Equation (52) is the expression of the modified wavenumber of the third-order FV-MLS method.

If we only consider the spatial discretization error, the numerical solution of (36) is:

$$\tilde{u}_I^{num} = \frac{g(0)}{i\kappa\Delta x} \left(e^{i\kappa(x_R - a^*t)} - e^{i\kappa(x_L - a^*t)} \right) \quad (53)$$

with $a^* = \frac{aZ_I}{i\kappa}$. Thus, we can write

$$\frac{a^*}{a} = \frac{Z^*}{i\kappa} \quad (54)$$

The modified phase velocity (a^*) is the numerical propagation velocity of a harmonic function. For example, if $\frac{a^*}{a} < 1$, the numerical propagation is slower than the real velocity. So, there are dispersion errors in the numerical solution. As the original equation is non-dispersive, the numerical solution of an harmonic function with different wavenumbers loses its original shape. For a non-harmonic problem, the crests of the waves propagate with the phase velocity but the energy of the wave packet propagate with the group velocity $v_g = a \frac{\partial \kappa^*}{\partial \kappa}$ (see [27]).

In figure 9 we plot the real part of the scaled modified wavenumber versus the real scaled wavenumber for different numerical methods. We observe that the third-order FV-MLS method presents a narrow range of frequencies whose error is below 0.1%, and a wide range of frequencies whose error is below 1%. We observe that the dispersion curves of the FV-MLS method with different kernels plotted in that figure are almost overlapped.

For the wave equation it is usual to represent the numerical phase and group velocities. These are plotted in figure 10. We see one of the effects of the bad resolution of the waves: the spurious parasitic waves. In figure 9 it is shown that a given modified wavenumber represents two discrete waves. One is related to low frequencies (physical) and other related to high frequencies (spurious). In the plot of group velocities 10 (right), we see that there exists

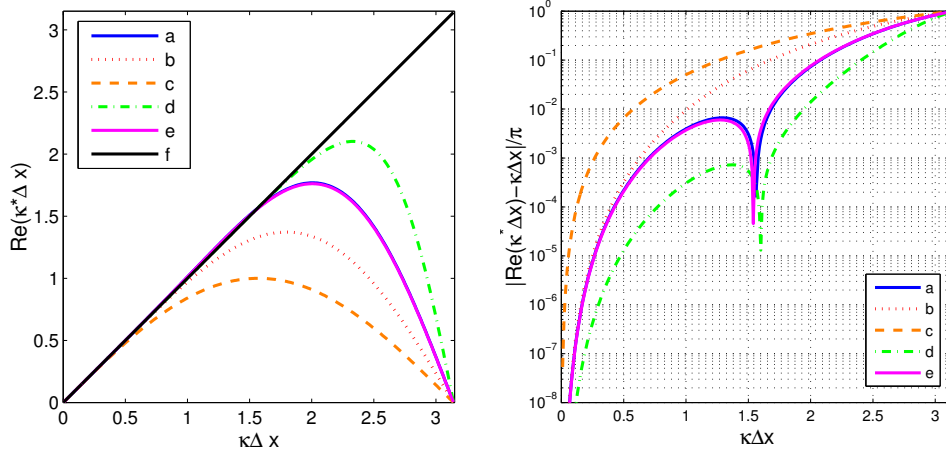


Figure 9: On the left, we plot the real part of $\kappa^* \Delta x$ versus $\kappa \Delta x$ for different numerical methods. On the right we show the dispersion error magnitude $(\text{Re}(k^* \Delta x) - \kappa \Delta x)/\pi$. The compared numerical methods are: (a) Third-order FV-MLS with exponential kernel and $s_x = 5$, (b) MLS approximation cubic basis and cubic spline kernel $k = 0.7$, (c) second-order centered finite differences, (d) fourth-order tridiagonal compact finite differences $\alpha = 5/14$ (see [2]), (e) Third-order FV-MLS with cubic spline kernel $k = 0.6$, (f) exact. Dispersion curves of schemes a and e are almost overlapped.

a wavenumber (different for each numerical scheme) for which the group velocity becomes negative. This parasitic wave propagates for the whole computational domain spoiling the numerical solution. As this parasitic wave could be supersonic, this behavior is expected even in supersonic flows, where propagation upstream is clearly non-physical.

As we said before, the imaginary part of the modified wavenumber (κ^*) is related to dissipation errors. The FV-MLS modified wavenumber presents a non-null imaginary part, due to the upwinding. Although this could be seen as a drawback in terms of accuracy, the greatest part of the dissipation is introduced in the scales that are wrongly resolved for the numerical method. This can be seen as an implicit filtering of the spurious waves, remaining unaffected the resolved scales.

If we compare the dispersion and dissipation curves of a second-order and a third-order scheme, plotted on figure 11, we see that the increase of accuracy of the numerical method is achieved by diminishing both, dispersion and dissipation errors. The dissipation introduced is considerably lower, and the range of frequencies well resolved also increases.

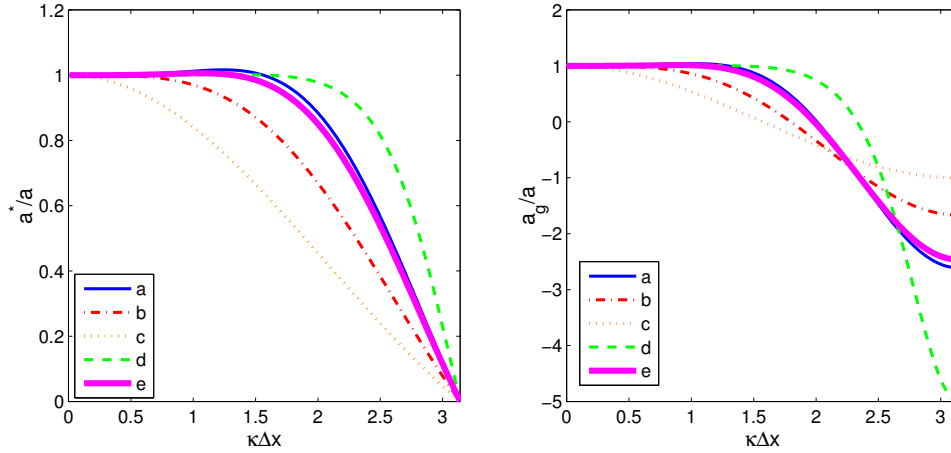


Figure 10: numerical phase speed (left) and numerical group velocity (right) for several numerical schemes. (a) Third-order FV-MLS with exponential kernel and $s_x = 5$, (b) MLS approximation cubic basis and cubic spline kernel $k = 0.7$, (c) second-order centered finite differences, (d) fourth-order tridiagonal compact finite differences $\alpha = 5/14$ (see [2]), (e) Third-order FV-MLS with cubic spline kernel $k = 0.6$

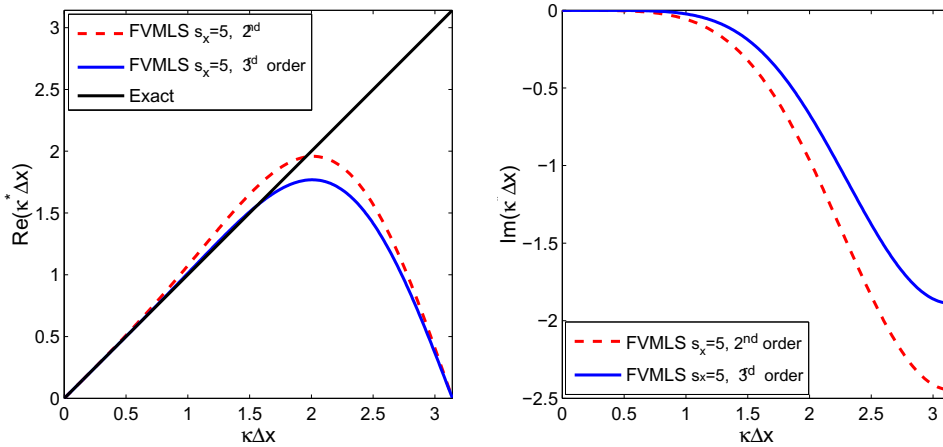


Figure 11: Influence of the order of the approximation for the FV-MLS method. On the left: Real part of $\kappa^*\Delta x$ versus $\kappa\Delta x$. On the right: Imaginary part of $\kappa^*\Delta x$ versus a $\kappa\Delta x$.

The number of *points per wavelength* (ppw) that a numerical scheme needs to approximate the exact wavenumber within a specified error tolerance is given by $\frac{2\pi}{\kappa\Delta x}$. Following [2] we define the *resolving efficiency* of a scheme as the fraction of the well-resolved waves, $ef = \frac{\kappa_c^*}{\pi}$, where (κ_c^*) define the shortest well-resolved wave. In table 1 we show the ppw for different schemes, for a given error tolerance $\epsilon = \frac{|\kappa_c^* - \kappa|}{\kappa}$. We also show the resolving efficiency of each scheme and the scaled wavenumber $(\kappa_c^*)\Delta x$. We note that the MLS approximation (polynomial cubic basis) has the same resolving efficiency than a fourth-order centered finite difference scheme.

Scheme	Tolerance (ϵ)								
	$\epsilon = 0.001$			$\epsilon = 0.005$			$\epsilon = 0.01$		
	ef	ppw	$\kappa_c^*\Delta x$	ef	ppw	κ_c^*	ef	ppw	$\kappa_c^*\Delta x$
a	0.02	78.5	0.08	0.05	36.96	0.17	0.08	26.18	0.24
b	0.13	15.32	0.41	0.2	10.13	0.62	0.24	8.37	0.75
c	0.13	15.32	0.41	0.2	10.13	0.62	0.24	8.37	0.75
d	0.52	3.81	1.65	0.56	3.54	1.77	0.59	3.38	1.86
e	0.14	13.96	0.45	0.23	8.73	0.72	0.29	6.90	0.91

Table 1: Resolving efficiency (ef), number of points per wavelength (ppw) and scaled wavenumber of the shortest well-resolved wave ($\kappa_c^*\Delta x$) for different numerical schemes for different tolerances ϵ . (a) Second-order centered finite differences, (b) fourth-order centered finite differences, (c) MLS approximation cubic basis and cubic spline kernel $k = 0.7$, (d) fourth-order tridiagonal compact finite differences $\alpha = 5/14$ (see [2]), (e) Third-order FV-MLS with exponential kernel and $s_x = 5$.

6. Influence of the kernel function on the properties of the FV-MLS method

In the previous section we have derived the expression (52), for the modified wavenumber of the third-order FV-MLS method in the case of the 1D

linear advection equation. This expression depends on the first derivatives of the MLS shape functions. In this section we examine the influence of the choice of the parameters of the kernel on the dispersion and dissipation properties of a MLS approximation, and then, we analyze the effect in the FV-MLS method.

6.1. MLS approximation

When we use a direct MLS discretization (for example, in the discretization of elliptic-like terms) we have seen that the dispersion characteristics of the MLS approximation are independent of the kernel parameters (for the *stencil* of the figure 1). Moreover, for the cubic spline kernel, there is no dissipation. This effect becomes clear if we examine the equation (22). Thus for the 5-point stencil, we write:

$$\begin{aligned}
 \kappa^* &= (-i) \sum_{l=-P}^Q \frac{\partial N_{I-l}}{\partial x} e^{i\kappa(l\Delta x)} = \\
 &= \sin(2\kappa\Delta x) \left(\frac{\partial N_{(I+2)}}{\partial x} - \frac{\partial N_{(I-2)}}{\partial x} \right) + \\
 &+ \sin(\kappa\Delta x) \left(\frac{\partial N_{(I+1)}}{\partial x} - \frac{\partial N_{(I-1)}}{\partial x} \right) - \\
 &- i \left[\cos(2\kappa\Delta x) \left(\frac{\partial N_{(I+2)}}{\partial x} + \frac{\partial N_{(I-2)}}{\partial x} \right) + \right. \\
 &\left. + \cos(\kappa\Delta x) \left(\frac{\partial N_{(I+1)}}{\partial x} + \frac{\partial N_{(I-1)}}{\partial x} \right) + \frac{\partial N_I}{\partial x} \right]
 \end{aligned} \tag{55}$$

where $(I-2)$, $(I-1)$, I , $(I+1)$, $(I+2)$ are referring to the cells of the stencil plotted in figure 1.

Recalling that the dispersion is related to the real part of the modified wavenumber, from equation (55) we see that the dispersion of the numerical scheme depends on the difference of the derivatives of the shape function in symmetric cells. If the kernel function and the stencil are symmetric, the value of this difference is independent of kernel parameters, and so the dispersion of the numerical scheme.

On the other hand, the dissipation is related to the imaginary part of the modified wavenumber. For the cubic spline kernel, $\frac{\partial N_I}{\partial x}$ is null (see figure 3), and for the given stencil $\frac{\partial N_{(I+i)}}{\partial x} = -\frac{\partial N_{(I-i)}}{\partial x}$. Then, the imaginary part

of the modified wavenumber is null and no dissipation is added for the numerical scheme (we remark that this conclusion is valid only for an uniform distribution of the grid nodes). This is not the situation of the exponential kernel, since $\frac{\partial N_I}{\partial x}$ is not null, as it was shown in figure 8. However, even although the value of the first derivative of the MLS-shape function is different for each value of s_x (see figure 1), the difference $\frac{\partial N_{(I+i)}}{\partial x} = -\frac{\partial N_{(I-i)}}{\partial x}$ remains constant (for the given stencil), and thus the dispersion for the stencil plotted in figure 1 is independent of the parameters of the kernel.

6.2. FV-MLS method for hyperbolic terms

In this section we examine the effect of the kernel parameters on the FV-MLS method for hyperbolic terms. In figures 12 and 13 we show the dispersion-dissipation curves and the phase speed and group velocity for different values of the shape parameter s_x of the exponential kernel. The results for the cubic spline kernel are drawn on figures 14 and 15. As we have mentioned before, the FV-MLS method is dissipative due to the upwinding. However, the amount of introduced dissipation depends on the value of the kernel parameters.

For the exponential kernel, the choice $s_x = 6$ introduce the minimum amount of dissipation. For the exponential kernel this happens for a value of the parameter of $k = 0.501$. These are the practical limits of the kernel parameter, since a lower value makes the moment matrix \mathbf{M} singular. On unstructured grids these values could be unattainable, because they may lead to a bad conditioning of the moment matrix. It is important to note that it is possible to develop very similar numerical schemes from different kernels, by selecting the right value of the parameter. This is important since the exponential kernel is more robust than the cubic spline on arbitrary meshes.

On the other hand, in tables 2 and 3 we show the resolving efficiency of the method FV-MLS for several values of the kernel parameters s_x and k . The influence of s_x is bigger than the influence of k . The value $k = 0.6$ yields the best results in terms of resolving efficiency for the cubic spline kernel. For the exponential kernel, the best resolving efficiency is obtained for $s_x = 6$, that also presents the less dissipative behavior. This fact may cause instabilities in certain problems, overall in Euler equations, where there is no dissipative terms that help to the stabilization. So, a recommended value for this kind of problems is $s_x = 1$ or $s_x = 5$. We note that the values for $s_x = 3$ and $s_x = 4$

are identical. This is due to the effect of the kernel derivatives previously commented on section 3. We check the change in the tendency of the curves by comparing the values for $s_x = 3$, $s_x = 3.5$ and $s_x = 4$.

We remark that the dissipation is introduced for the numerical scheme in the range of bad-resolved waves, so it dims the spurious waves generated by the numerical scheme. From this point of view, we could consider this as a low-pass filtering. This *implicit* filtering acts similarly to the *explicit* filters developed for finite difference methods [2, 4].

	$\epsilon = 0.001$			$\epsilon = 0.005$			$\epsilon = 0.008$			$\epsilon = 0.01$		
s_x	ef	ppw	$\kappa_c^* \Delta x$	ef	ppw	$\kappa_c^* \Delta x$	ef	ppw	$\kappa_c^* \Delta x$	ef	ppw	$\kappa_c^* \Delta x$
1	0.13	15.32	0.41	0.20	9.82	0.64	0.23	8.61	0.73	0.25	7.95	0.79
2	0.12	16.11	0.39	0.19	10.30	0.61	0.22	8.98	0.70	0.24	8.49	0.74
3	0.12	16.98	0.37	0.18	11.02	0.57	0.21	9.67	0.65	0.22	9.11	0.69
3.5	0.11	17.45	0.36	0.18	11.21	0.56	0.20	9.81	0.64	0.22	9.23	0.68
4	0.12	16.98	0.37	0.18	11.02	0.57	0.21	9.67	0.65	0.22	9.11	0.69
5	0.14	13.96	0.45	0.23	8.73	0.72	0.27	7.48	0.84	0.29	6.90	0.91
6	0.20	10.13	0.62	0.40	5.07	1.24	0.41	4.87	1.29	0.42	4.76	1.32

Table 2: Resolving efficiency of the third-order FV-MLS method for different tolerances ϵ and different values of s_x .

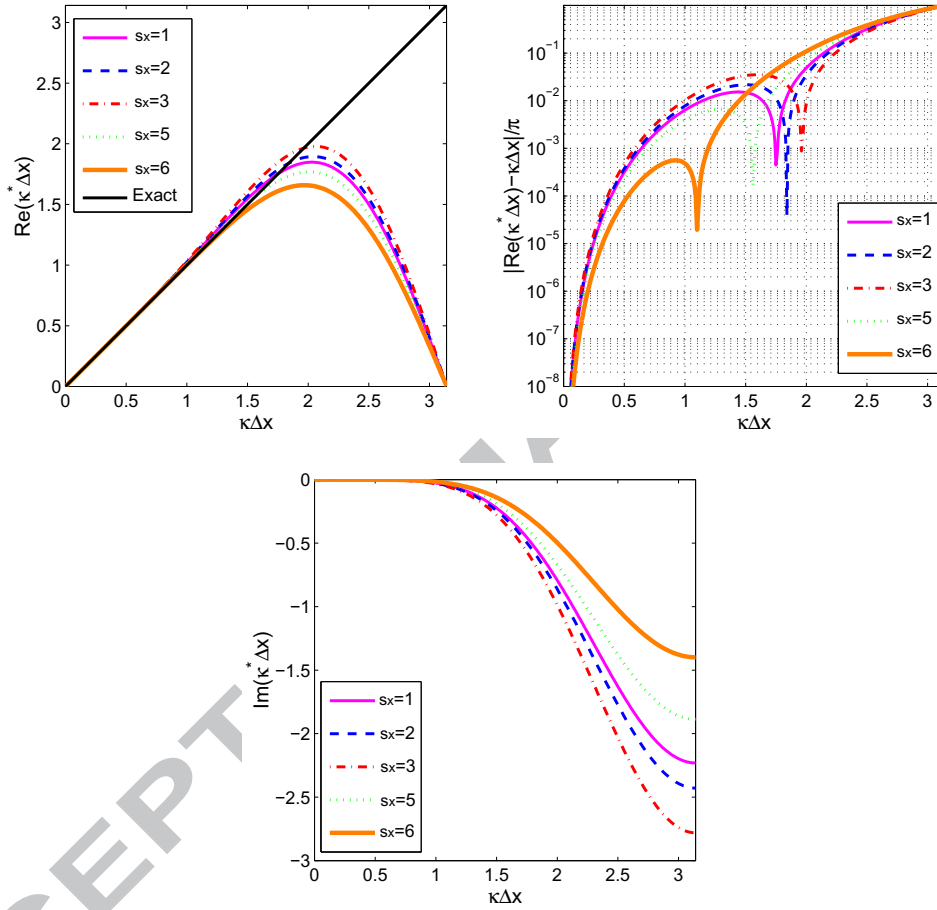


Figure 12: Dispersion and dissipation curves of the third-order FV-MLS method for different values of the kernel shape parameter s_x . On the top, we plot the real part of the modified scaled wavenumber, related to the dispersion of the numerical scheme (left) and the dispersion error in logarithmic scale (right). On the bottom, we plot the imaginary part of the modified scaled wavenumber, related to dissipation.

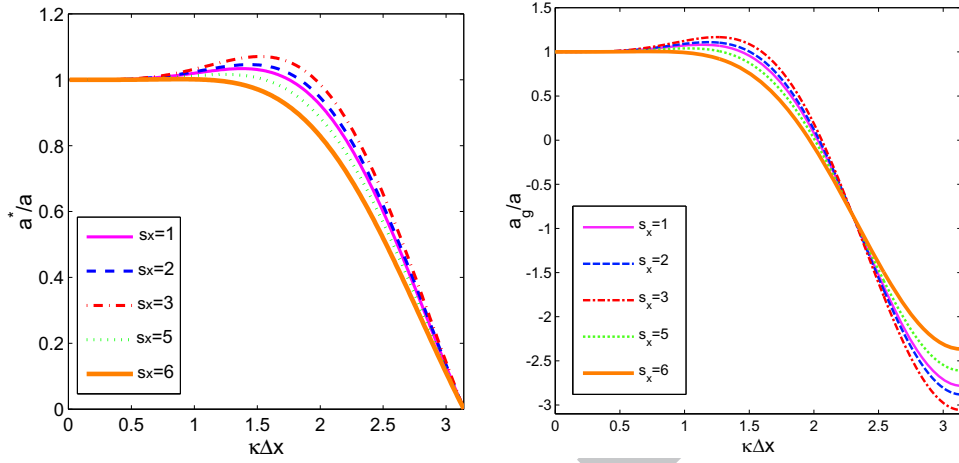


Figure 13: Phase-speed (left) and group velocity (right) of the third-order FV-MLS method for different values of the kernel shape parameter s_x .

k	$\epsilon = 0.001$			$\epsilon = 0.005$			$\epsilon = 0.008$			$\epsilon = 0.01$		
	ef	ppw	$\kappa_c^* \Delta x$	ef	ppw	$\kappa_c^* \Delta x$	ef	ppw	$\kappa_c^* \Delta x$	ef	ppw	$\kappa_c^* \Delta x$
0.501	0.23	8.73	0.72	0.38	5.33	1.18	0.40	5.07	1.24	0.40	4.95	1.27
0.52	0.23	8.85	0.71	0.38	5.28	1.19	0.40	5.02	1.25	0.41	4.91	1.28
0.6	0.17	12.08	0.52	0.29	6.98	0.90	0.46	4.39	1.43	0.46	4.33	1.45
0.7	0.15	13.66	0.46	0.23	8.61	0.73	0.27	7.31	0.86	0.30	6.76	0.93
0.8	0.14	14.28	0.44	0.22	8.85	0.71	0.26	7.76	0.81	0.28	7.14	0.88
1	0.14	14.61	0.43	0.22	9.24	0.68	0.25	7.95	0.79	0.27	7.39	0.85

Table 3: Resolving efficiency of the third-order FV-MLS method for different tolerances ϵ and different values of k .

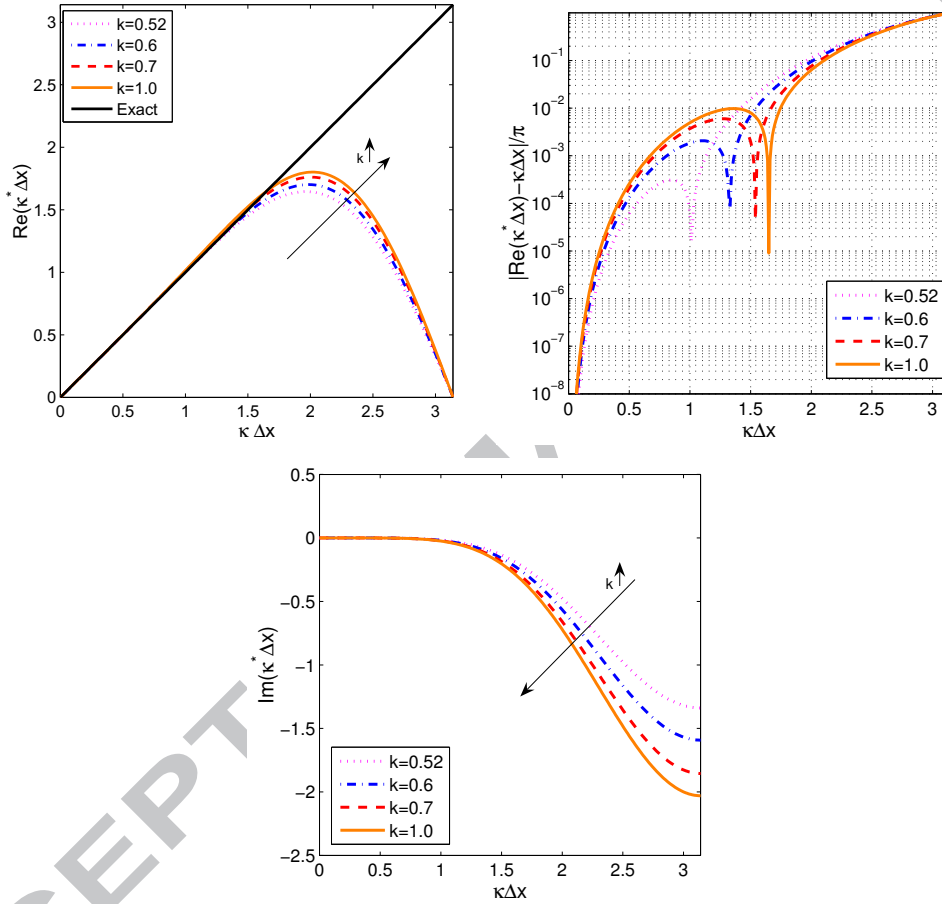


Figure 14: Dispersion and dissipation curves of the third-order FV-MLS method for different values of the cubic spline kernel parameter k . On the top, we plot the real part of the modified scaled wavenumber, related to the dispersion of the numerical scheme (left) and the dispersion error in logarithmic scale (right). On the bottom, we plot the imaginary part of the modified scaled wavenumber, related to dissipation

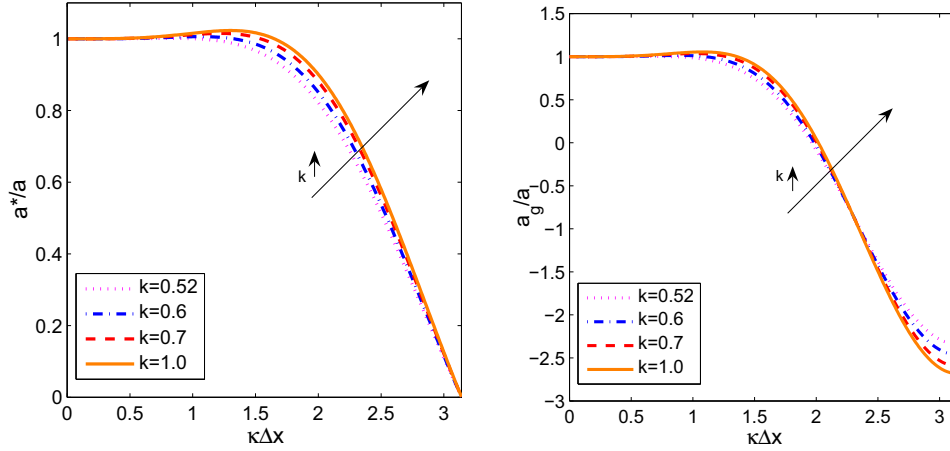


Figure 15: Phase-speed (left) and group velocity (right) of the third-order FV-MLS method for different values of the cubic spline kernel parameter k .

6.2.1. Analysis of the complete discretization

In previous sections, we have analyzed the behavior of the spatial discretization for direct approximations with MLS and for the finite volume-based method FV-MLS. In this section we introduce the effect of the time integration. We consider an explicit Runge-Kutta time integration.

Equation (30) indicates that the exact solution of (23) may be decomposed in both an spatial and a temporal part. With a Runge-Kutta method, we approximate the temporal part of (23) with a Taylor expansion. Following to [28, 29] we write the equation (23) as:

$$\frac{\partial u}{\partial t} = qu \quad (56)$$

where $q = -ia\kappa$ is complex. We define the *amplification factor* of a Runge-Kutta method as

$$r(z) = \frac{u^{n+1}}{u^n} \quad (57)$$

thus, introducing (29), the exact amplification factor is

$$r_e(z) = \frac{u^{n+1}}{u^n} = \frac{g(0)e^{i\kappa(x-a(t+\Delta t))}}{g(0)e^{i\kappa(x-at)}} = e^{-ia\kappa\Delta t} = e^z \quad (58)$$

with $z = -ia\kappa\Delta t = q\Delta t$.

on the other hand, if q is a linear operator, a fourth-order Runge-Kutta method applied to the equation (23) reads as:

$$u_j^1 = u_j^n + \frac{1}{4}qu_j^n\Delta t \quad (59)$$

$$u_j^2 = u_j^n + \frac{1}{3}qu_j^1\Delta t \quad (60)$$

$$u_j^3 = u_j^n + \frac{1}{2}qu_j^2\Delta t \quad (61)$$

$$u_j^{n+1} = u_j^n + qu_j^3\Delta t \quad (62)$$

Upper index 1, 2 and 3 refer to intermediate steps in the time marching process, and n and $n + 1$ refer to the solution in time n and $n + 1$.

From equation (62), and knowing that $z = q\Delta t$, we write,

$$u_j^{n+1} = u_j^n \left(1 + z + \frac{1}{2}z^2 + \frac{1}{6}z^3 + \frac{1}{24}z^4 \right) \quad (63)$$

Then, the amplification factor for a fourth-order Runge-Kutta method is

$$r(z) = \left(1 + z + \frac{1}{2}z^2 + \frac{1}{6}z^3 + \frac{1}{24}z^4 \right) \quad (64)$$

These are the first terms of a Taylor expansion of e^z . This result can be written in a more general form for any Runge-Kutta method [29].

Thus, $r(z)$ is a complex number that we write as:

$$r(z) = |r(z)| e^{i\alpha(\kappa)} \quad (65)$$

Following [30], the numerical dissipation is given by the magnitude of the amplification factor. When $|r(z)| \leq 1$ the method is stable. On the other hand, $\alpha(\kappa)$ represents the dispersion of the numerical scheme.

From (58) and (65) we obtain $\alpha = a\kappa^*\Delta t$. We represent the dispersion with the parameter $\alpha^* = \frac{\alpha}{CFL}$, where CFL is the Courant-Friedrichs-Lewy number $CFL = \frac{a\Delta t}{\Delta x}$, since

$$\alpha^* = \frac{\alpha}{CFL} = \frac{a\kappa^*\Delta t\Delta x}{a\Delta t} = \kappa^*\Delta x \quad (66)$$

We remark that in $r(z)$ is also included the spatial discretization. Thus, the dispersion and dissipation curves obtained in this section represent the complete discretization.

For the FV-MLS method, from (36) and (49), we know that:

$$\frac{\partial \tilde{u}_I}{\partial t} = \frac{-ag(t)}{i\kappa\Delta x} (e^{i\kappa x_R} - e^{i\kappa x_L}) Z^* \quad (67)$$

and recalling from (33) that:

$$\frac{\partial \tilde{u}_I}{\partial t} = -aZ^*\tilde{u}_I \quad (68)$$

we obtain from (56) and from the relation $z = q\Delta t$:

$$z = -aZ^*\Delta t \quad (69)$$

Figures 16, 17, 18 and 19 show the influence of temporal discretization on the dispersion and dissipation curves of the third-order FV-MLS scheme, for a fourth-order (RK4) and a third-order (RK3) Runge-Kutta method. In figure 20 we compare the dispersion error for different values of the kernel parameters.

The choice of kernel parameters affects greatly to the stability of the numerical method. Moreover, the choice of the time step and the order of the RK method affect to the spectral resolution of the method.

For a RK4 time integration scheme we obtain the following criteria for the stability of the third-order FV-MLS method: For the exponential kernel,

$$\begin{aligned} CFL < 1.4 \quad s_x = 1 \\ CFL < 1.6 \quad s_x = 6 \end{aligned} \quad (70)$$

whereas for the cubic spline kernel, $CFL < 1.6$.

For a RK3 time integration method: For the exponential kernel,

$$\begin{aligned} CFL < 1.2 \quad s_x = 1 \\ CFL < 1.6 \quad s_x = 6 \end{aligned} \quad (71)$$

whereas for the cubic spline kernel.

$$\begin{aligned} CFL < 1.6 \quad k = 0.52 \\ CFL < 1.4 \quad k = 0.6 \end{aligned} \quad (72)$$

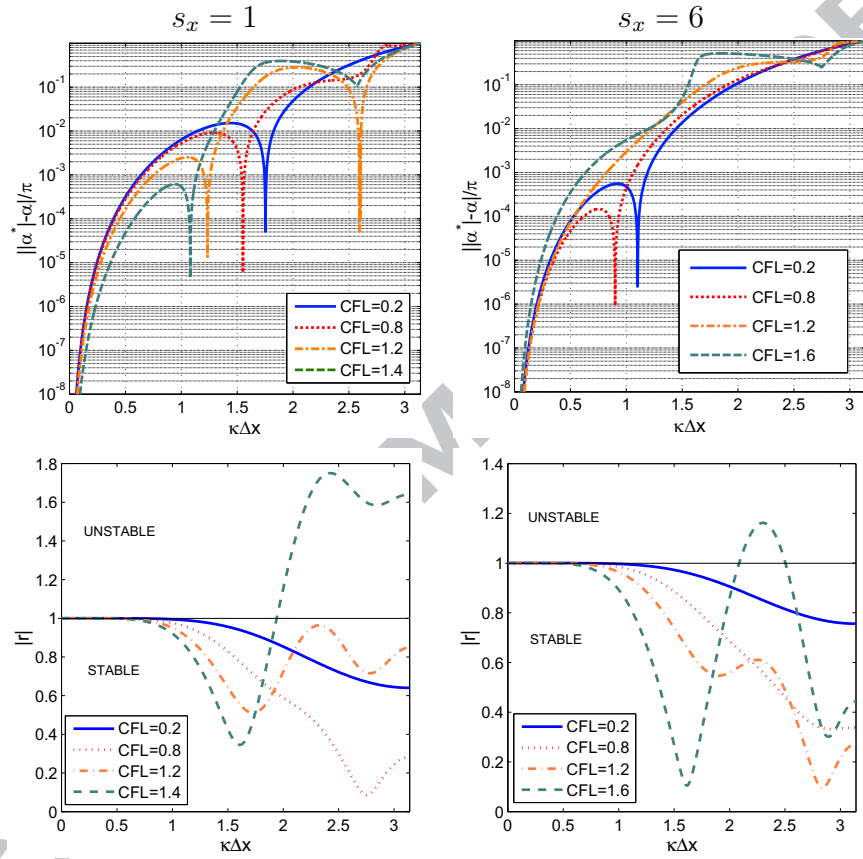


Figure 16: Dispersion error $\frac{\|\alpha^* - \alpha\|}{\pi}$ (top), and dissipation (bottom) for the third-order FV-MLS method, exponential kernel $s_x = 1$ (left column) and $s_x = 6$ (right column), with a fourth-order Runge-Kutta method for different CFL.

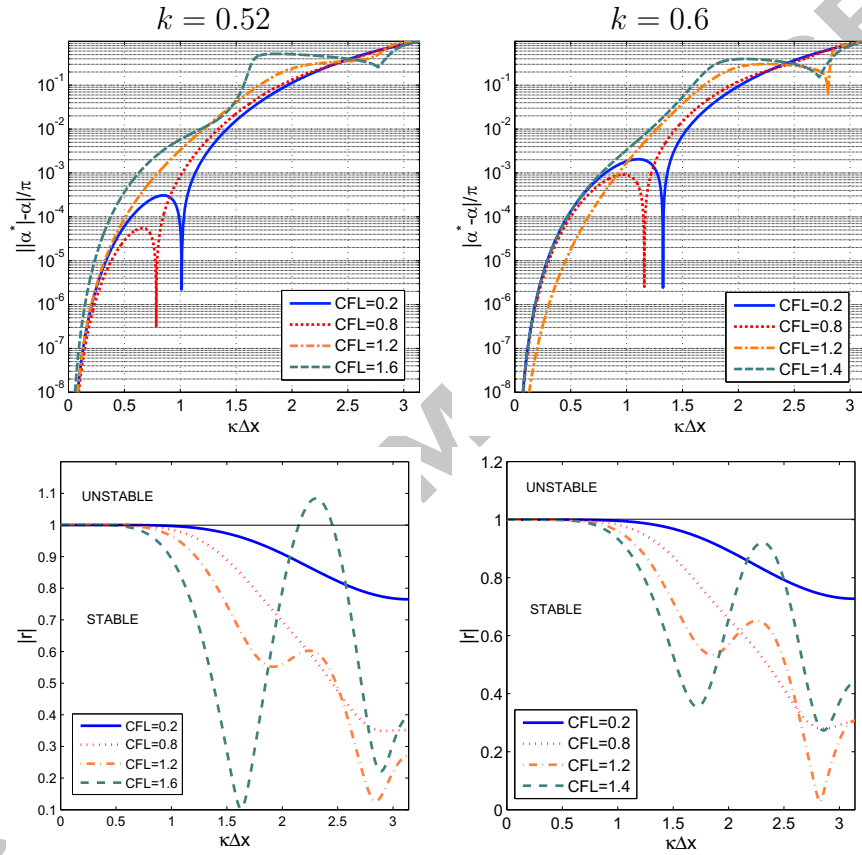


Figure 17: Dispersion error $\frac{\|\alpha^* - \alpha\|}{\pi}$ (top), and dissipation (bottom) for the third-order FV-MLS method, cubic spline kernel $k = 0.52$ (left column) and $k = 0.6$ (right column), with a fourth-order Runge-Kutta method for different CFL.

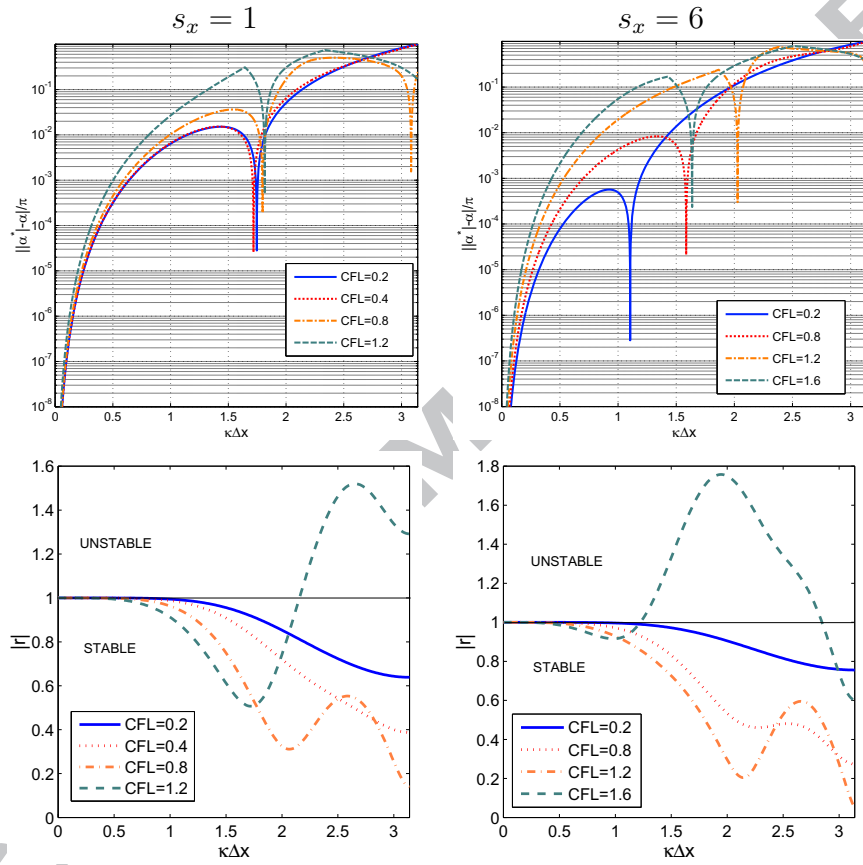


Figure 18: Dispersion error $\frac{||\alpha^* - \alpha||}{\pi}$ (top), and dissipation (bottom) for the third-order FV-MLS method, exponential kernel $s_x = 1$ (left column) and $s_x = 6$ (right column), with a third-order Runge-Kutta method for different CFL.

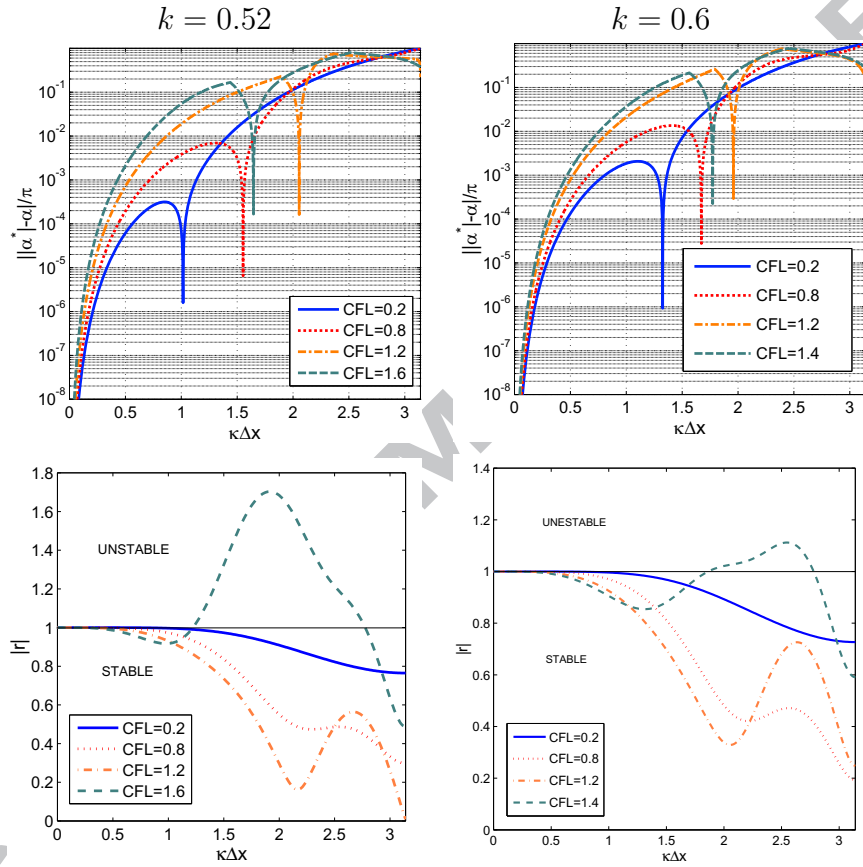


Figure 19: Dispersion error $\frac{\|\alpha^* - \alpha\|}{\pi}$ (top), and dissipation (bottom) for the third-order FV-MLS method, cubic spline kernel $k = 0.52$ (left column) and $k = 0.6$ (right column), with a third-order Runge-Kutta method for different CFL.

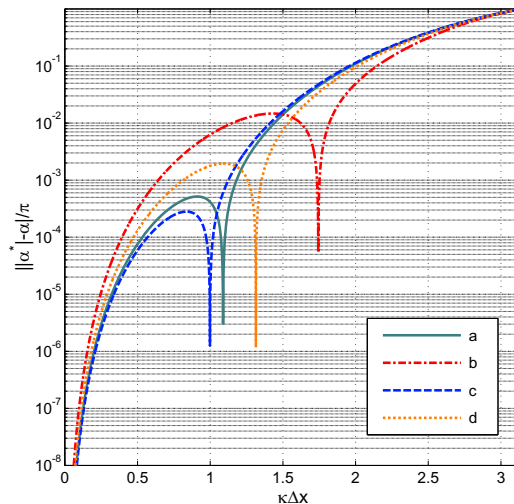


Figure 20: Comparison between the dispersion error $\frac{\|\alpha^* - \alpha\|}{\pi}$ for the third-order FV-MLS scheme with RK4 for $CFL=0.4$: (a) exponential kernel $s_x = 6$, (b) exponential kernel $s_x = 1$, (c) cubic spline kernel $k = 0.52$, (d) cubic spline kernel $k = 0.6$.

However, the accuracy of the method is greatly affected for $CFL > 0.8$. We note that dispersion errors for the wavenumber region between $[1, 1.5]$ are bigger with the RK3 scheme. For such wavenumbers the dissipation for these wavenumbers may be not enough to completely dissipate the spurious waves. Thus, it is recommended the use of CFL numbers lower than 0.8 with the Runge-Kutta schemes tested. This restriction becomes more important if the RK3 scheme is used.

With this choice of CFL, the wavenumber region $[0, \frac{\pi}{2}]$ suffers from little dispersive error, for both, exponential and cubic kernels with RK4 and RK3 time integration schemes. The dispersion error is lower when the RK4 scheme is used, for a given kernel parameter. This is shown in figure 21. The dissipation introduced for the numerical scheme is similar for low CFL numbers, but the trend is better when RK4 scheme is used, in the sense that the amount of dissipation introduced is bigger for the highest wavenumbers. Thus, RK4 scheme seems to be the best choice.

We have also tested an optimized RK method (Low Dispersion and Dissipation RK LDDRK) [31] but there is no any substantial difference in comparison with a standard RK method. A similar effect has been reported for *Dispersion-Relation Preserving* (DRP) schemes [3]. In these methods the increase in the accuracy of the solution is reported from a six-order spa-

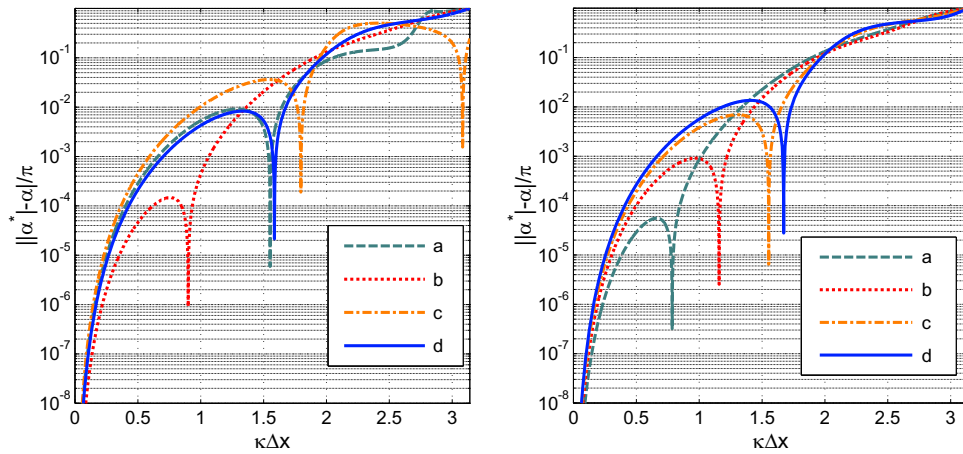


Figure 21: Comparison between the dispersion error $\frac{||\alpha^* - \alpha|}{\pi}$ for the third-order FV-MLS scheme with RK4 and RK3 for CFL=0.8. On the left exponential kernel: (a) RK4 $s_x = 1$, (b) RK4 $s_x = 6$, (c) RK3 $s_x = 1$, (d) RK3 $s_x = 6$. On the right, cubic kernel: (a) RK4 $k = 0.52$, (b) RK4 $k = 0.6$, (c) RK3 $k = 0.52$, (d) RK3 $k = 0.6$.

tial discretization [32]. This fact suggests the possibility of developing an optimized RK algorithm for the FV-MLS method.

7. Numerical Examples

7.1. One-dimensional linear wave equation

In this section we solve the first problem presented in the *First ICASE/LaRC Workshop on Benchmark Problems in Computational Aeroacoustics* [33]. We solve the equation (23) with the following initial condition:

$$u(x, 0) = 0.5e^{[-\ln(2)(\frac{x}{3})^2]} \quad (73)$$

The transported wave may be considered as the addition of a number of harmonic waves with different frequencies and amplitudes. If the numerical scheme is not able to solve waves with very different frequencies the numerical solution will be a very distorted wave. The computational domain is $-20 \leq x \leq 450$ and we plot the results at non-dimensional times $t = 100$, $t = 400$.

In figures 22, 23, 24, 25 we plot the results for the third-order FV-MLS method. For $\Delta x = 1$ the solution is somewhat dissipative, and the wave shape presents a certain amount of distortion for $t = 400$ (see figure 22 and

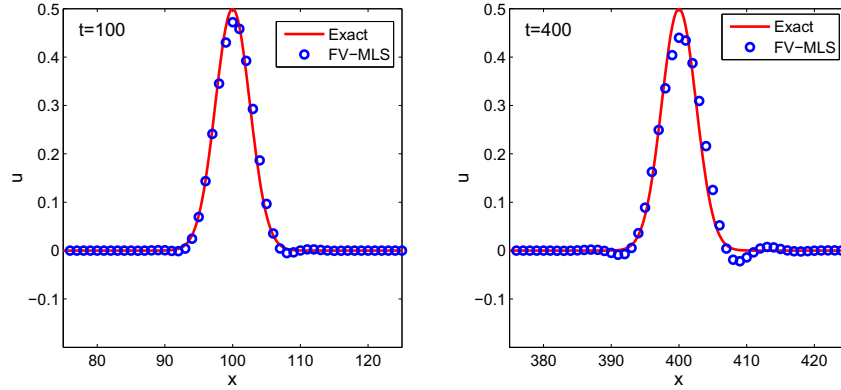


Figure 22: Third-order FV-MLS solution for the first problem presented in [33] at different non-dimensional times, with $CFL = 0.6$, $\Delta x = 1$, exponential kernel (15) $s_x = 6$.

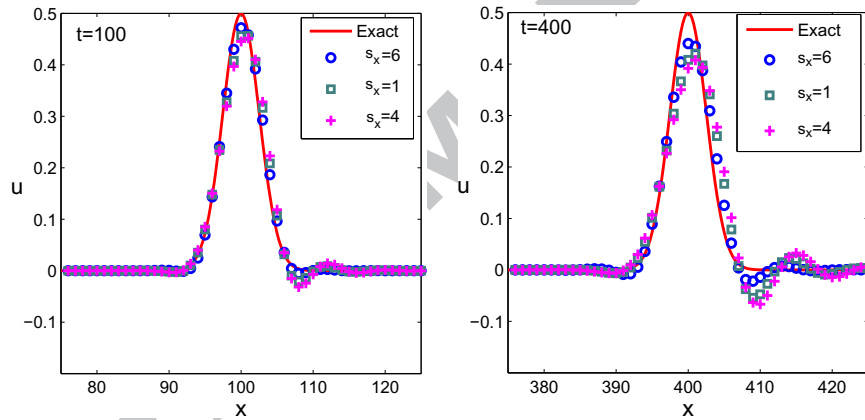


Figure 23: Third-order FV-MLS solution for the first problem presented in [33] at different non-dimensional times, with $CFL = 0.6$, $\Delta x = 1$, exponential kernel (15) and several values of the shape parameter s_x .

23 for the exponential kernel results and figure 24 for the cubic spline kernel). However, the dispersion and dissipation errors of the wave are smaller than other higher-order methods as the as the fourth-order MacCormac method presented in [34], or fourth-order centered finite differences [35]. As it is expected, the solution improves as we decrease the grid spacing. Figure 25 shows the results for $\Delta x = 0.25$. In figure 26 we also show the results for the second order FV-MLS method. It is clear the benefit of using the third-order FV-MLS method.

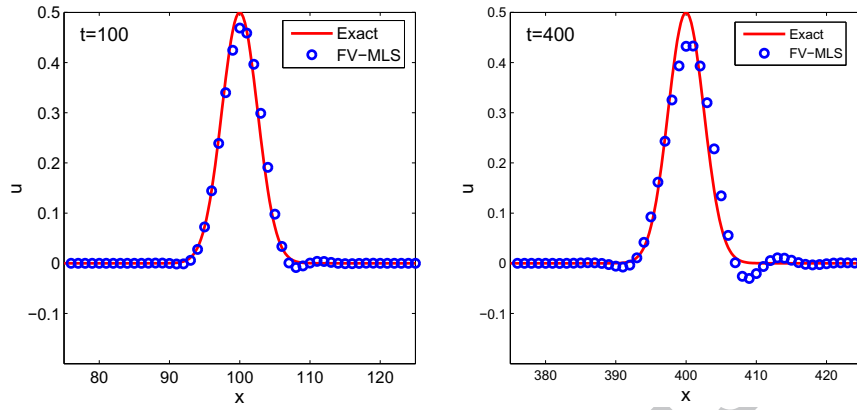


Figure 24: Third-order FV-MLS solution for the first problem presented in [33] at different non-dimensional times, with $CFL = 0.6$, $\Delta x = 1$, cubic spline kernel (13) $k = 0.6$.

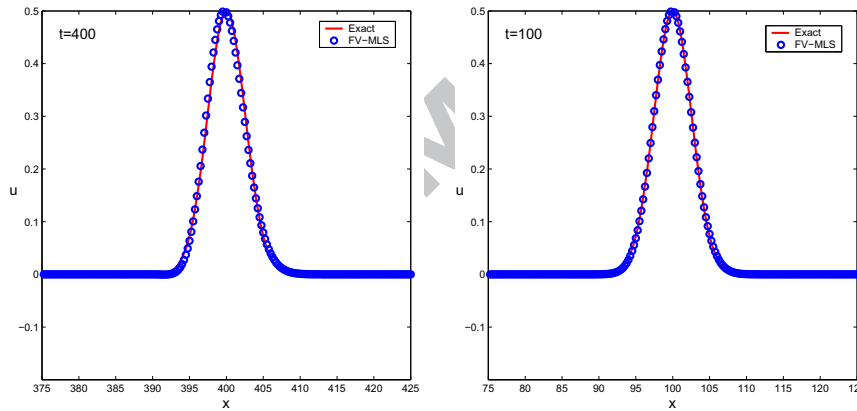


Figure 25: Third-order FV-MLS solution for the first problem presented in [33] at different non-dimensional times, with $CFL = 0.6$, $\Delta x = 0.25$, exponential kernel (15) and $s_x = 6$.

7.2. One-dimensional nonlinear wave equation

In this section we solve the 1D non-linear equation:

$$\frac{\partial u}{\partial t} + u \frac{\partial u}{\partial x} = 0 \quad (74)$$

that, written in conservative form reads:

$$\frac{\partial u}{\partial t} + \frac{1}{2} \frac{\partial u^2}{\partial x} = 0 \quad (75)$$

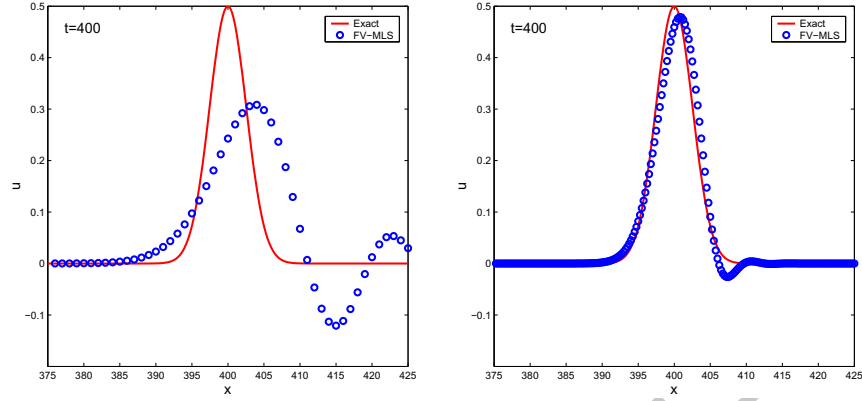


Figure 26: Second-order FV-MLS solution for the first problem presented in [33] at a non-dimensional time $t = 400$, with $CFL = 0.6$, exponential kernel (15) $s_x = 6$, $\Delta x = 1$ (left) and $\Delta x = 0.25$ (right).

on the domain $-4 \leq x \leq 10$, with initial condition:

$$u(x, 0) = \begin{cases} 0, & x \leq 0 \\ 1, & x > 0 \end{cases} \quad (76)$$

The exact solution for this problem is:

$$u(x, t) = \begin{cases} 0, & x \leq 0 \\ \frac{x}{t}, & 0 < x < t \\ 1, & x > t \end{cases} \quad (77)$$

In figure 27 we plot the results for the third-order FV-MLS method and several grid sizes with the exponential kernel and $s_x = 1$, at $t = 3$. The results improve as the grid size is decreased. This results agree with those of the compact finite volume DRP and OPC (Optimized Prefactored Compact) schemes [19]. The results of the FV-MLS method are noticeably better than the results obtained by DRP and OPC finite difference schemes [19, 36]. This example shows the availability of the FV-MLS method to handle strong gradients.

7.3. Wave scattering by a complex geometry.

The objective of this example is to verify the generalization of the conclusions obtained from the one-dimensional analysis of the advection equation to the analysis of a more complex problem. Here we propose to solve the 2D

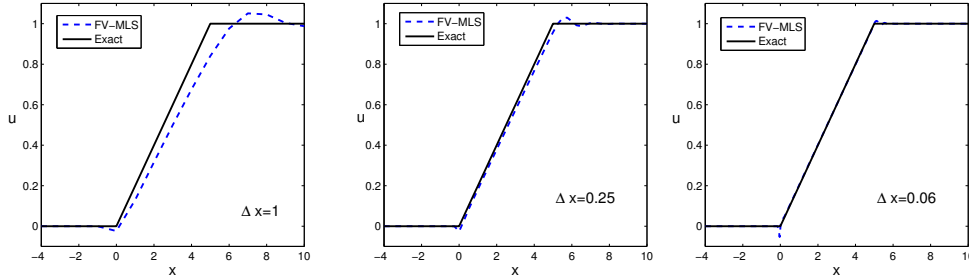


Figure 27: Third-order FV-MLS solution for the first problem presented in [33] at $t = 3$, with $CFL = 0.6$, and different grid spacing, exponential kernel (equation (15)), $s_x = 1$.

Linearized Euler Equations (LEE) in complex geometry using the proposed formulation (the whole set of these commonly used equations can be found in [37]). A previous work has been done by the authors [38] and [39] concerning the application of FV-MLS to CAA problems on unstructured grids. We have shown that FV-MLS is very well adapted to solve LEE with a very good accuracy. Here, among several examples presenting acoustic wave propagation in complex geometries, we choose the test case of wave scattering by the NASA's 30P30N airfoil [40].

The main acoustic noise source for this airfoil is the one generated by the vortex shedding at the trailing edge of the upstream part, called slat noise. To simulate the slat noise we place an artificial acoustic source at $(x_{sc}, y_{sc}) = (-0.012, 0.01)$ defined as: $S = \exp(-((x - x_{sc})^2 + (y - y_{sc})^2)/b^2) \times \sin(\omega t) \times [0, 0, 0, 1]^T$ where the angular frequency is $\omega = 6\pi$, $b = 0.003$ and t is the time coordinate. The source term is made dimensionless with $[\rho_0 c_0 / \Delta x, 0, 0, \rho_0 c_0^3 / \Delta x]^T$. In this expression, ρ_0 is the mean value of the density of the stationary solution and c_0 is the mean value of the speed of sound. For seek of simplicity we choose an angular frequency ($\omega = 6\pi$). This value permits us to use a moderate grid size, since the objective here is only to compare two configurations with two different kernel function parameters s . The leading edge of the main part of the airfoil is placed at $(0, 0)$.

The discretization has been performed in order to guarantee a minimum number of 6 cells per wavelength around the airfoil. A detail of the grid is shown in figure 28.

The exponential kernel has been selected for this example, and the CFL number for the computations is 0.2. The results are presented at $t = 3$ units in figure (29) for $s_x = s_y = 1$. We observe that pressure waves originated at

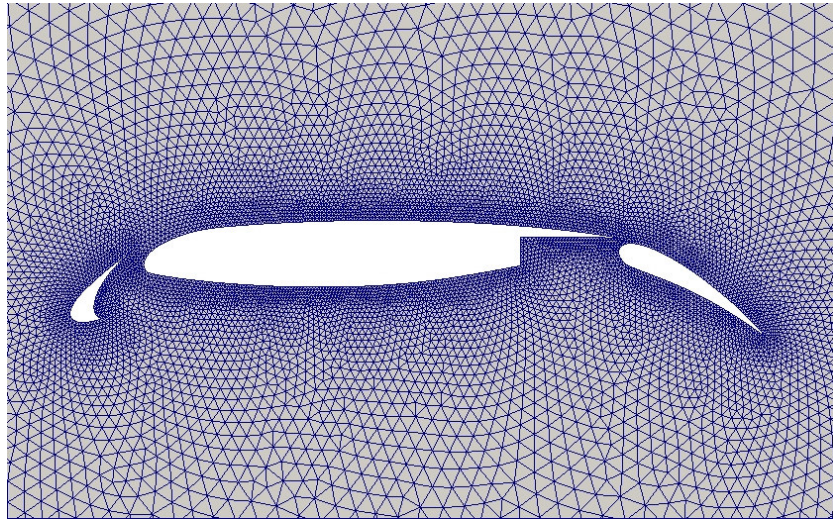


Figure 28: Detail of the unstructured grid used for the wave scattering problem.

the source point propagate radially without any appreciable dispersion error in the directions free of obstacles. On the other hand, waves propagating in the direction of the airfoil are scattered.

In figure (30) we show the time variation of the acoustic pressure at points A(0,0.3), B(0,-0.3), C(1.23,0.07) and D(1.15,-0.48) for $s_x = s_y = 1$ and $s_x = s_y = 5$.

Note that the results for $s = s_x = s_y = 5$ are clearly more dissipative than those obtained for $s = s_x = s_y = 1$. Moreover, we observe a slight difference in the phase of the pressure waves. This is related with the different dispersion curves of the numerical scheme for each value of the parameter s . We also note that even though the 2D Linearized Euler Equations are not the simple 2D extension of the 1D advection equation and an unstructured grid has used, the conclusions obtained from the 1D advection equation still hold for this more complex case.

8. Conclusions

In this work we perform an analysis of the influence of the kernel parameters on the behavior of a high-order finite volume method based on Moving Least squares approximations. First, we obtain an analytical expression of the modified wavenumber of the numerical scheme, and then we examine the

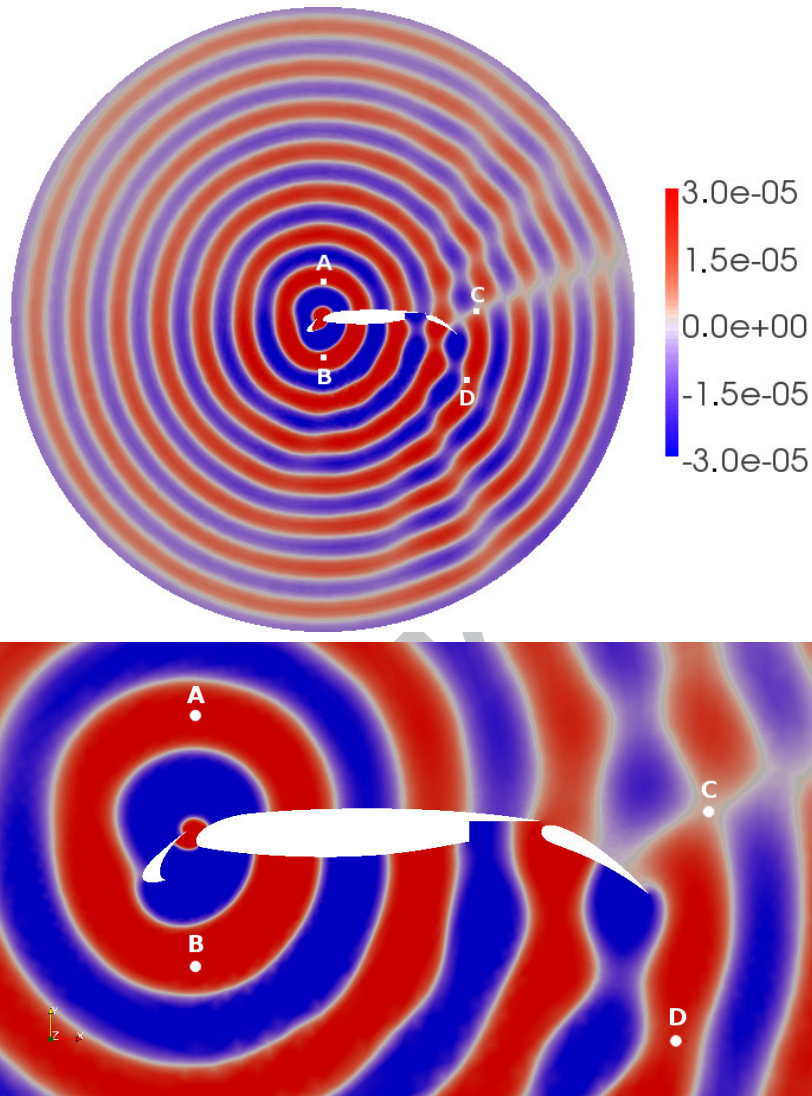


Figure 29: Acoustic pressure distribution at $t = 3$ for the wave scattering problem. General view and detail of the profile, with the points A, B, C and D where the acoustic pressure is measured continuously (figure 30).

influence of the parameters of the kernel function on the dispersion and dissipation characteristics of the third-order FV-MLS method. We examine the discretization of elliptic-like terms with a direct MLS approximation. The discretization of hyperbolic terms is performed by examination of the 1D linear advection equation. We have focused our attention in two kernel func-

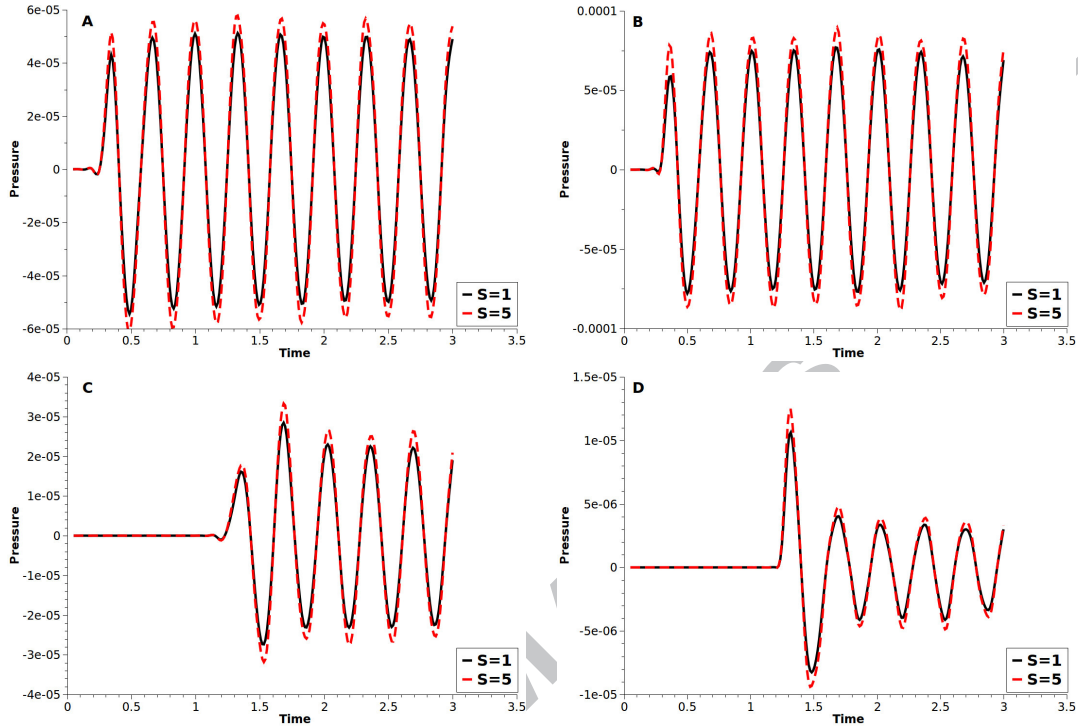


Figure 30: Time variation of the acoustic pressure at points A(0,0.3), B(0,-0.3), C(1.23,0.07) and D(1.15,-0.48) for $s = s_x = s_y = 1$ and $s = s_x = s_y = 5$.

tions: the exponential kernel and the cubic spline kernel. The third-order FV-MLS method, presents a more dissipative behavior when used with the exponential kernel than when the cubic spline kernel is chosen. However, it is possible to obtain methods with very similar characteristics by choosing the adequate kernel parameter. This feature is important since the shape variation as we change the value of the parameter is bigger for the exponential kernel than for the cubic spline kernel. This characteristic of the exponential kernel represents an advantage in terms of robustness in arbitrary meshes. In this kind of meshes, and for the same spatial resolution, the FV-MLS method presents a similar accuracy than other higher-order methods as for example, the Discontinuous Galerkin method [22], but without the addition of new degrees of freedom.

We have also examined the influence of time integration when explicit Runge-Kutta methods are used. We present the result for a RK4 and a RK3 explicit method. The FV-MLS method is more stable when a fourth-order

1
2
3
4
5
6
7
8
9
10
11
12
13
14
15
16
17
18
19
20
21
22
23
24
25
26
27
28
29
30
31
32
33
34
35
36
37
38
39
40
41
42
43
44
45
46
47
48
49
50
51
52
53
54
55
56
57
58
59
60
61
62
63
64
65

Runge-Kutta method is used. The results clearly show a significant improvement of dispersion and dissipation properties of the numerical method if the third-order FV-MLS scheme is used compared with the second-order one. Moreover, with the explicit fourth-order Runge-Kutta scheme the dispersion error is lower than with the third-order Runge-Kutta scheme, whereas the dissipation error is similar for both time-integration schemes. A value of the CFL number lower than 0.8 is required in order to obtain a low dispersion error. CFL numbers higher than 0.8 lead to unacceptable dispersion errors, especially with the RK3 scheme. The use of optimized RK schemes as the LDDRK does not improve the results.

It is clear than the present analysis only holds for uniform nodal distribution. Thus, in non-uniform nodal distributions the dispersion and dissipation curves will be different for each distribution of nodes. However, the dependency of the characteristics of the numerical method with the kernel parameter opens the possibility of a local optimization on unstructured grids, to compute the value of the kernel parameter for a given distribution of the points of the stencil that obtains the best possible characteristics of the numerical scheme.

We have applied the method to the resolution of the one-dimensional linear and non-linear wave equation. The results shows the availability of the FV-MLS method to deal with wave propagation problems when large gradients are involved. For the test case of the 1D non-linear wave equation, results of the third-order FV-MLS method are noticeably better than the results obtained by DRP and OPC finite difference schemes. The results for the 1D linear wave equation are more accurate than other higher-order methods commonly used in literature, as the fourth-order MacCormac method or fourth-order centered finite differences. In order to enlarge the validity of the present analysis to more dimensions and more general grids we have solved the 2D Linearized Euler Equations in a complex domain using a triangular grid. The results keep the trend observed in 1D. The dissipation is increased when the kernel parameter changes from $s_x = s_y = 5$ to $s_x = s_y = 1$ and there is a slight phase difference. This example also shows the promising capabilities of the FV-MLS method for its application to aeroacoustics.

The present study only holds for the third-order FV-MLS. However, in our opinion the conclusions obtained remain for higher-order FV-MLS discretizations, provided the kernel function is the same. However, at the present time we cannot affirm this conclusion categorically, and more research is in progress. Moreover, the author's opinion is that the present analysis also

holds for other 1D models governed by different equations if the nature of the equations is the same than the ones examined here. Thus for elliptic equations the conclusions of the MLS approximations holds, and for hyperbolic equations the conclusions obtained for the FV-MLS method will be valid.

Acknowledgments

The authors are grateful to Dr. Mehdi R. Khorrami from Computational Aerosciences Branch, NASA Langley Research Center, for kindly giving us the airfoil geometry. This work has been partially supported by the *Ministerio de Educación y Ciencia* of the Spanish Government (#DPI2007-61214 and #DPI2009-14546-C02-01), cofinanced with FEDER funds and the *Secretaría Xeral de I+D* of the *Xunta de Galicia* (Grants #PGDIT09MDS00718PR and #PGDIT09REM005118PR).

References

- [1] Syy, W., A study of finite difference approximations to steady-state, convection-dominated flow problems, *Journal of Computational Physics* 57:415-438, 1985.
- [2] Lele, S. K., *Compact Finite Difference Schemes with Spectral-like Resolution*, *Journal of Computational Physics* 103:16-42, 1992.
- [3] Tam, C. K. W. and Webb, J. C., *Dispersion-Relation-Preserving Finite Difference Schemes for Computational Acoustics*, *Journal of Computational Physics*, 107:262-281, 1993.
- [4] Gaitonde, D. V., Visbal, M. R., *High-Order Schemes for NavierStokes Equations: Algorithm and Implementation into FDL3DI*, U.S. Air Force Research Lab., TR AFRL-VA-WP-TR-1998-3060, WrightPatterson AFB, OH, 1998.
- [5] Visbal, M. R. and Gaitonde, D. V., *High-Order-Accurate Methods for Complex Unsteady Subsonic Flows*, *AIAA Journal*, 37(10):1231-1239, 1999.
- [6] Visbal, M. R. and Rizzeta, D. P., *Large-Eddy simulation on Curvilinear Grids Using Compact Differencing and Filtering Schemes*, *Journal of Fluids Engineering*, 124:836-847, 2002.

- 1
2
3
4
5
6
7
8
9 [7] Barth, T. J., Jespersen, D. C., *The design and application of upwind*
10 *schemes on unstructured meshes*, AIAA-89-0366, 1989.
11
12 [8] Barth, T. J., Frederickson, P. O., *Higher-order solution of the Euler equa-*
13 *tions on unstructured grids using quadratic reconstruction*, AIAA paper
14 90-0013, 1990.
15
16 [9] Jahawar, P., Kamath, H., *A high-resolution procedure for Euler and*
17 *Navier-Stokes computations on unstructured grids*, Journal of Computa-
18 tional Physics 164:165-203, 2000.
19
20 [10] Barth, T. J., *Recent developments in high order k-exact reconstruction*
21 *on unstructured meshes*, AIAA paper 93-0068, 1993.
22
23 [11] Bassi, F., Rebay, S., *A higher-order accurate discontinuous finite el-*
24 *ement solution of the 2D Euler equations*, Journal of Computational
25 Physics, 138:251-285, 1997.
26
27 [12] Bassi, F., Rebay, S., *A higher-order accurate discontinuous finite ele-*
28 *ment method for the numerical solution of the compressible Navier-Stokes*
29 *equations*, Journal of Computational Physics, 131:267-279, 1997.
30
31 [13] Cockburn, B., Shu C.-W., *Runge-Kutta discontinuous Galerkin meth-*
32 *ods for convection dominated problems*, Journal on Scientific Computing,
33 16:173-261, 2001.
34
35 [14] Dolejší, V., *On the discontinuous Galerkin method for the numerical so-*
36 *lution of the Navier-Stokes equations*, International Journal for Numerical
37 Methods in Fluids, 45:1083-1106, 2004.
38
39 [15] Persson, P., Peraire, J., *An efficient low memory implicit DG algo-*
40 *rithm for time dependent problems*, 44th AIAA Aerospace Sciences Meet-
41 ing, AIAA-2006-0113, Reno, Nevada, 2006.
42
43 [16] Deconinck, H., Paillère, H., Struijs, R., Roe, P. L., *Multidimensional Up-*
44 *wind Schemes based on Fluctuation-Splitting for Systems of Conservation*
45 *Laws*, Computational Mechanics, 11:323-340, 1993.
46
47 [17] Wang, Z. J., *Spectral (finite) volume method for conservation laws on*
48 *unstructured grids*, Journal of Computational Physics 178:210-251, 2002.
49
50
51
52
53
54
55
56
57
58
59
60
61
62
63
64
65

- 1
2
3
4
5
6
7
8
9 [18] Codina, R, *Finite element approximation of the hyperbolic wave equation*
10 *in mixed form*, Computer Methods in Applied Mechanics and Engineering,
11 *197(13-16):1305-1322*, 2008
12
13
14 [19] Popescu, M., Shyy, W., Garbey, M., *Finite volume treatment of*
15 *dispersion-relation-preserving and optimized prefactored compact schemes*
16 *for wave propagation*, Journal of Computational Physics *210:705-729*,
17 2005.
18
19
20 [20] Cueto-Felgueroso, L., Colominas, I., Nogueira, X., Navarrina, F.,
21 Casteleiro, M., *Finite volume solvers and Moving Least-Squares ap-*
22 *proximations for the compressible Navier-Stokes equations on unstruc-*
23 *tured grids*, Computer Methods in Applied Mechanics and Engineering,
24 *196:4712-4736*, 2007.
25
26
27 [21] Cueto-Felgueroso, L., Colominas, I., *High-order Finite Volume methods*
28 *and multiresolution reproducing kernels*, Archives of Computational Meth-
29 *ods in Engineering*, *15(2):185-228*, 2008.
30
31
32 [22] Nogueira, X., Cueto-Felgueroso, L., Colominas, I., Gómez, H., Navar-
33 *rina, F., Casteleiro, M., On the accuracy of Finite Volume and Dis-*
34 *continuous Galerkin discretizations for compressible flow on unstructured*
35 *grids*, International Journal for Numerical Methods in Engineering, , DOI:
36 *10.1002/nme.2538*, 2009.
37
38
39 [23] Cueto-Felgueroso, L., Colominas, I., Fe, J., Navarrina, F., Casteleiro,
40 M., *High order finite volume schemes on unstructured grids using Mov-*
41 *ing Least Squares reconstruction. Application to shallow waters dynamics*,
42 International Journal for Numerical Methods in Engineering, *65:295-331*,
43 2006.
44
45
46 [24] Cueto-Felgueroso, L., Peraire, J., *A time-adaptive finite volume method*
47 *for the CahnHilliard and KuramotoSivashinsky equations*, Journal of Com-
48 *putational Physics*, *227(24):9985-10017*, 2008.
49
50
51 [25] Lancaster, P., Salkauskas, K., *Surfaces generated by moving least squares*
52 *methods*, Mathematics of Computation *37(155):141158*, 1981.
53
54
55 [26] Liu, G. R., and Liu, M. B., *Smoothed Particle Hydrodynamics. A mesh-*
56 *free particle method*, Singapore: World Scientific Publishing, 2003
57
58
59
60
61
62
63
64
65

- 1
2
3
4
5
6
7
8
9 [27] Bailly, C., Bogey, C., *An overview of numerical methods for acoustic*
10 *wave propagation*, European Conference on Computational Fluid Dynam-
11 ics, ECCOMAS CFD, P. Wesseling, E. Oñate, J. Périaux (Eds), 2006.
12
13 [28] Jameson, A., Baker, T. J., *Solution of the Euler Equations for Complex*
14 *Configurations*, AIAA paper 83-1929, 1983.
15
16 [29] Stanescu, D., Habashi, W. G., *2N-Storage Low Dissipation and Disper-*
17 *sion Runge-Kutta Schemes for Computational Acoustics*, Journal of Com-
18 putational Physics, 143:674-681, 1998.
19
20 [30] Yu, S.-T, Hsieh, K.-C. and Peter Tsai, Y.-L., *Simulating Waves in*
21 *Flows by Runge-Kutta and Compact Difference Schemes*, AIAA Journal,
22 33(3):421-429, 1995.
23
24 [31] Hu, F. Q., Hussaini M. Y., Manthey, J. L., *A Low-Dissipation and Low*
25 *Dispersion Runge-Kutta Schemes for Computational Acoustics*, Journal of
26 Computational Physics 124:177-191, 1996.
27
28 [32] Wagner, C., Hüttl, T., Sagaut, P. (eds.), *Large-Eddy Simulation for*
29 *Acoustics*, Cambridge Aerospace Series, Cambridge: Cambridge University
30 Press, 2007.
31
32 [33] Hardin, J. C., Ristorcelli, J. R., and Tam C. K. W., *ICASE/LaRC*
33 *workshop on benchmark problems in computational aeroacoustics*, NASA
34 Conference Publication 3300, 1995.
35
36 [34] Viswanathan, K., Sankar, L. N., *A comparative study of upwind and*
37 *MacCormack schemes for CAA benchmark problems*, ICASE/LaRC Work-
38 shop on Benchmark Problems in computational aeroacoustics, 185-195
39 ,1995
40
41 [35] Tam, C. K. W. and Shen, H., *Direct Computation of Nonlinear Acoustic*
42 *Pulses using High Order Finite Difference Schemes*, AIAA paper 93-4325,
43 1993.
44
45 [36] Ashcroft, G., Zhang, X., *Optimized prefactored compact scheme*, Journal
46 of Computational Physics 190:459-477, 2003.
47
48 [37] Hu, F. Q., *On Absorbing Boundary Conditions for Linearized Euler*
49 *Equations by a Perfectly Matched Layer*, Journal of Computational Physics
50 129:201-219, 1996.
51
52
53
54
55
56
57
58
59
60
61
62
63
64
65

- 1
2
3
4
5
6
7
8
9 [38] Nogueira, X., Cueto-Felgueroso, L., Colominas, I., Khelladi, S.,
10 Navarrina, F., Casteleiro, M., *Resolution of Computational Aeroa-*
11 *coustics problems on unstructured grids with a higher-order finite vol-*
12 *ume scheme*, Journal of Computational and Applied Mathematics,
13 DOI:10.1016/j.cam.2009.08.067, 2009.
14
15
16 [39] Khelladi, S., Nogueira, X., Bakir, F., Cueto-Felgueroso, L., Colominas,
17 I., *Finite Volume Solvers and Moving Least Squares approximations for*
18 *the Linearized Euler equations on unstructured grids*, The Journal of the
19 Acoustical Society of America, 123(5),3381, 2008.
20
21
22 [40] Singer, B. A., Lockard, D. P., Brentner, K. S., Khorrami, M. R., Berk-
23 man, M. E., Choudhari, M., *Computational Aeroacoustic Analysis of Slat*
24 *Trailing-Edge Flow*, AIAA paper 99-1802, 1999.
25
26
27
28
29
30
31
32
33
34
35
36
37
38
39
40
41
42
43
44
45
46
47
48
49
50
51
52
53
54
55
56
57
58
59
60
61
62
63
64
65